Journal Pre-proof

Integrative imaging reveals SARS-CoV-2 induced reshaping of subcellular morphologies

Mirko Cortese, Ji-Young Lee, Berati Cerikan, Christopher J. Neufeldt, Viola M.J. Oorschot, Sebastian Köhrer, Julian Hennies, Nicole L. Schieber, Paolo Ronchi, Giulia Mizzon, Inés Romero Brey, Rachel Santarella-Mellwig, Martin Schorb, Mandy Boermel, Karel Mocaer, Marianne S. Beckwith, Rachel M. Templin, Viktoriia Gross, Constantin Pape, Christian Tischer, Jamie Frankish, Natalie K. Horvat, Vibor Laketa, Megan Stanifer, Steeve Boulant, Alessia Ruggieri, Laurent Chatel-Chaix, Yannick Schwab, Ralf Bartenschlager

Please cite this article as: Cortese, M., Lee, J.-Y., Cerikan, B., Neufeldt, C.J., Oorschot, V.M.J., Köhrer, S., Hennies, J., Schieber, N.L., Ronchi, P., Mizzon, G., Brey, I.R., Santarella-Mellwig, R., Schorb, M., Boermel, M., Mocaer, K., Beckwith, M.S., Templin, R.M., Gross, V., Pape, C., Tischer, C., Frankish, J., Horvat, N.K., Laketa, V., Stanifer, M., Boulant, S., Ruggieri, A., Chatel-Chaix, L., Schwab, Y., Bartenschlager, R., Integrative imaging reveals SARS-CoV-2 induced reshaping of subcellular morphologies, *Cell Host and Microbe* (2020), doi: https://doi.org/10.1016/j.chom.2020.11.003.

SARS-CoV-2

Lung Epithelial Cell

SARS-CoV-2
Infected Lung Cell

Withaferin A

Paclitaxel

FIB-SEM

Electron tomography

- Nucleus
- Golgi
- Peroxisomes
- Cytoskeleton
- Double Membrane Vesicles
- Viral Replication Organelles

Integrative imaging reveals SARS-CoV-2 induced reshaping of subcellular morphologies

Mirko Cortese[1,*], Ji-Young Lee[1,10], Berati Cerikan[1], Christopher J. Neufeldt[1], Viola M. J. Oorschot[3], Sebastian Köhrer[2,14], Julian Hennies[2,4], Nicole L. Schieber[2], Paolo Ronchi[3], Giulia Mizzon[2,3], Inés Romero Brey[2], Rachel Santarella-Mellwig[3], Martin Schorb[3], Mandy Boermel[3], Karel Mocaer[2], Marianne S. Beckwith[2], Rachel M. Templin[2], Viktoriia Gross[2], Constantin Pape[5,6], Christian Tischer[7], Jamie Frankish[8], Natalie K. Horvat[6,9] Vibor Laketa[10], Megan Stanifer[1], Steeve Boulant[11,12], Alessia Ruggieri[1], Laurent Chatel-Chaix[13], Yannick Schwab[2,3,*], Ralf Bartenschlager[1,10,15,*,§]

1 Department of Infectious Diseases, Molecular Virology, Heidelberg University, 69120 Heidelberg, Germany

2 Cell Biology and Biophysics Unit, European Molecular Biology Laboratory, 69117 Heidelberg, Germany

3 Electron Microscopy Core Facility, European Molecular Biology Laboratory, 69117 Heidelberg, Germany

4 Collaboration for joint PhD degree between EMBL and Heidelberg University, Faculty of Biosciences, Heidelberg, Germany

5 IWR, Heidelberg University, Heidelberg, Germany

6 European Molecular Biology Laboratory (EMBL), 69117 Heidelberg, Germany

7 Center for Bioimage Analysis, European Molecular Biology Laboratory, Heidelberg, Germany

8 BioMed X Institute, BioMed X GmbH, 69120 Heidelberg, Germany

9 Molecular Medicine Partnership Unit (MMPU), Otto-Meyerhof-Zentrum, Im Neuenheimer Feld 350, 69120 Heidelberg, Germany

10 German Center for Infection Research, Heidelberg partner site, Heidelberg, Germany

11 Research Group "Cellular polarity and viral infection", German Cancer Research Center (DKFZ), 69120 Heidelberg, Germany

12 Department of Infectious Diseases, Virology, Heidelberg University, 69120 Heidelberg, Germany

13 Institut National de la Recherche Scientifique, Centre Armand-Frappier Santé Biotechnologie, 531, Boulevard des Prairies Laval, Québec, QC, H7V 1B7, Canada

14 Clinical Cooperation Unit Molecular Hematology/Oncology, German Cancer Research Center (DKFZ), 69120 Heidelberg, Germany

15 Division Virus-Associated Carcinogenesis, German Cancer Research Center (DKFZ), 69120 Heidelberg, Germany

§ Lead Contact: ralf.bartenschlager@med.uni-heidelberg.de

*Correspondence to: mirko.cortese@med.uni-heidelberg.de; yannick.schwab@embl.de; ralf.bartenschlager@med.uni-heidelberg.de

1

Summary

Pathogenesis induced by SARS-CoV-2 is thought to result from both an inflammation dominated cytokine response and virus-induced cell perturbation causing cell death. Here, we employ an integrative imaging analysis to determine morphological organelle alterations induced in SARS-CoV-2 infected human lung epithelial cells. We report 3D electron microscopy reconstructions of whole-cells and subcellular compartments, revealing extensive fragmentation of the Golgi apparatus, alteration of the mitochondrial network and recruitment of peroxisomes to viral replication organelles formed by clusters of double-membrane vesicles (DMVs). These are tethered to the endoplasmic reticulum, providing insights into DMV biogenesis and spatial coordination of SARS-CoV-2 replication. Live cell imaging combined with an infection sensor reveals profound remodeling of cytoskeleton elements. Pharmacological inhibition of their dynamics suppresses SARS-CoV-2 replication. We thus report insights into virus-induced cytopathic effects, and provide alongside a comprehensive publicly available repository of 3D data-sets of SARS-CoV-2 infected cells for download and smooth online visualization.

Keywords

INTRODUCTION

As of end of September 2020, the ongoing COVID-19 pandemic has caused almost one million fatalities and has affected more than 30 million individuals with confirmed infection worldwide (https://covid19.who.int/). While a second wave of infections is occuring in many countries, the severe acute respiratory syndrome coronavirus 2 (SARS-CoV-2), the etiologic agent of this disease, is expected to become seasonal. Thus, there is an urgent need to develop and implement both prophylactic and therapeutic strategies against this virus. Tremendous efforts are being deployed to rapidly develop a safe-guarding vaccine with no less than 150 candidates currently under evaluation. Hence, much attention has been drawn to the study of virion structure and potential surface epitopes relevant for induction of neutralizing antibodies (Chu et al., 2020; Wrapp et al., 2020). In stark contrast, much less is known about how SARS-CoV-2 drives pathogenesis, but it is becoming clear that disease severity is determined by two parameters. These are a predominantly inflammatory cytokine response triggered by the virus and direct cytopathogenicity of SARS-CoV-2, leading to death of infected cells by a so far poorly characterized mechanism (Chu et al., 2020; Huang et al., 2020; Tang et al., 2020). Knowledge about viral cytopathogenicity requires detailed insights into how SARS-CoV-2 replicates in and alters its host cell. Information gained in this area is expected to foster the development of innovative therapy mitigating disease severity. However, thus far such insights have been mostly inferred from studies on related betacoronaviruses such as the highly pathogenic Middle East respiratory syndrome coronavirus (MERS-CoV) and SARS-CoV-1, the mouse hepatitis virus (MHV) model system or some endemic coronaviruses causing common cold. While some approved drugs are considered for repurposing strategies (e.g. hydroxychloroquine, lopinavir/ritonavir) because of their antiviral activity in cell culture, the clinical benefit of these drugs in terms of survival outcome and severity of symptoms is disputed (Marzolini et al., 2020). Hence, there is a need to better understand the biological mechanisms driving the SARS-CoV-2 replication cycle in order to identify therapeutic targets and develop highly efficient drugs suppressing viral replication and virus-induced cell death.

Following viral entry initiated by the binding of Spike (S) viral protein to cell surface receptors, the best-studied one being angiotensin I converting enzyme 2 (ACE2), and S processing by cellular proteases (Hoffmann et al., 2020), the 30 kb-long positive-strand RNA genome is released into the cytoplasm. There, the two large open reading frames, 1a and, via ribosomal

86 frameshifting, 1a/b are translated giving rise to the replicase (rep) polyproteins rep1a and

87 rep1a/1b, respectively. These viral products are cleaved by viral proteases to generate 16 mature

88 nonstructural proteins (nsps), most of them constituting the replication/transcription complex

89 responsible for viral RNA synthesis. During replication, several sub-genomic RNA species are

90 generated encoding for 4 structural proteins and multiple accessory proteins. The structural

91 proteins membrane (M), nucleocapsid (N), envelope (E) and S, together with the genomic RNA

92 drive the assembly of new virus particles, which in the case of other coronaviruses bud into the

93 endoplasmic reticulum-Golgi intermediate compartment (ERGIC). Virions are transported

94 through the secretory pathway and are released out of the cell (Perlman and Masters, 2020).

95 Like all positive-strand RNA viruses (Paul and Bartenschlager, 2013), SARS-CoV-2 induces a

96 remodeling of cellular endomembranes to form viral replication organelles (vROs). These

97 structures are thought to create a microenvironment conducive to RNA synthesis by allowing the

98 enrichment of metabolites, viral enzymes and cofactors, and by protecting viral RNA from

99 degradation and sensing by pattern recognition receptors of the innate immune system.

100 Coronavirus replication organelles are composed predominantly of double-membrane vesicles

101 (DMVs) that are most likely derived from the endoplasmic reticulum (ER) (Klein et al., 2020;

102 Knoops et al., 2008; Snijder et al., 2020). The interior of these structures contains double-

103 stranded (ds)RNA, the presumed viral replication intermediate, and *de novo* synthesized RNA,

104 demonstrating that DMVs are the sites of viral RNA synthesis. Consistently, a pore-like opening

105 spanning the two membrane layers of DMVs has been reported very recently, consistent with

106 release of newly synthesized RNA from the DMV interior into the cytoplasm (Wolff et al., 2020).

107 While these studies show that SARS-CoV-2 infection induces DMV formation as sites of viral

108 RNA replication, the biogenesis of these structures and their link to subcellular compartments is

109 poorly defined. Moreover, although SARS-CoV-2 infection is highly cytopathic, the impact of

110 the virus on integrity and morphology of cellular organelles has not been established.

111 In this study, we employed a combination of light and electron microscopy approaches to obtain

112 an integrative view of the 3D architecture of SARS-CoV-2 induced vROs, their inter-relation

113 with subcellular compartments and the impact of viral infection on cellular organelles. We show

114 whole-cell 3D reconstructions demonstrating profound morphological remodeling of multiple

115 membranous organelles such as fragmentation of the Golgi and recruitment of peroxisomes to

116 vROs. In addition, using live cell imaging in combination with a sensor monitoring productive
117 infection and replication, we show that DMV clusters are delimited by a reorganized "cage-like"
118 vimentin network and that pharmacological inhibition of this blocks viral replication. *In cellulo*
119 electron tomography and FIB-SEM data unveiled a network of interconnected DMVs that are
120 tethered to the ER by membrane connectors, providing insights into DMV biogenesis and their
121 role in coordinating the different steps of SARS-CoV-2 replication. Taken together, our study
122 provides a comprehensive 3D view of the SARS-CoV-2 replication cycle and alterations of
123 cellular organelles most likely contributing to cytopathogenicity of the virus and possibly serving
124 as target for urgently needed therapeutic strategies.

125

Results

127 **Kinetics of viral replication organelle formation in SARS-CoV-2 infected human**
128 **pulmonary epithelial cells**

129 Human pulmonary epithelial Calu-3 cells are known to be permissive to SARS-CoV-2 and hence
130 were used as model system to study the morphological remodeling of the cell induced by viral
131 infection. From 6 h postinfection onwards, SARS-CoV-2 positive cells as well as intra- and
132 extracellular viral RNA and infectious virus released into the cell culture supernatant became
133 detectable (Figures 1A-E). Thus, a full replication cycle can be completed within less than 6 h in
134 Calu-3 cells. At 12 and 24 h postinfection, the number of infected cells increased up to 70%
135 (Figure 1B), concomitant with an increase of intra- and extracellular viral RNA as well as virus
136 titers as determined by infectivity assay (Figures 1C-E). Ultrastructural analysis performed by
137 transmission electron microscopy (TEM) revealed a parallel appearance of DMVs, becoming
138 detectable as sporadic clusters of small-sized DMVs (diameter 185 nm ± 28 nm) at 6 h
139 postinfection and increasing in abundance and diameter (298 nm ± 42 nm) until 24 h
140 postinfection (Figures 1F and 1G). In some cases, large areas covered with glycogen granules, in
141 close proximity of lipid droplets, and membranous cisternae were present within infected cells
142 (Figure 1F (ii) lower panel and (iii), middle panel). Virions assembling within the Golgi
143 compartments as well as few extracellular virions were observed, starting at 6 h postinfection and
144 also increasing in abundance at later time points (Figure 1F (ii) upper panel and (iv), right panel).

145   Notably, ER tubules with collapsed luminal space were frequently observed in close proximity to

146   DMVs (Figure 1F (iii), right panel). Such structures are reminiscent of the so-called "zippered

147   ER" or "convoluted membranes" observed in cells infected with other coronaviruses (Snijder et

148   al., 2020). In some instances, these structures appear to connect the rough ER to the DMVs

149   (Figure 1F (i), lower left panel and 1F (iii), right panel).

150

151   **Whole cell volume 3D analysis reveals tight association of DMVs with an ER-based network**

152   **in SARS-CoV-2 infected cells**

153   To obtain a global view of the cellular alterations induced by SARS-CoV-2 infection, we applied

154   focused ion beam-scanning electron microscopy (FIB-SEM) analysis on infected Calu-3 cells.

155   The full volumes of three infected cells (infection being determined by the presence of DMVs),

156   and two mock-inoculated cells that served as reference, were acquired (the complete data sets are

157   made available for download on EMPIAR – ID 10490, and are viewable in an interactive manner

158   via MoBIE – see Star Methods and Table S1). Subsequently, we applied a bottom-up approach,

159   efficiently combining semi-automated and automated segmentation based on the multicut

160   pipeline (Beier et al., 2017) (see Star Methods) to achieve deep-segmentation of the dataset

161   (Figure 2; Figure S1; Video S1). Using this method, in which a small fraction of one dataset is

162   employed to train a machine learning-based approach for the recognition of defined and known

163   organelles, we segmented the cellular elements from one infected cell and one mock cell,

164   including the nucleus, the mitochondrial network and ER, as well as viral elements, such as the

165   DMVs and DMVs-associated ER membranes (Figure 2B-D; Figure S1; Video S1). In addition,

166   manual segmentation was applied for the Golgi apparatus in the infected cell (Figures 2B and 2C)

167   and some instances in the mock cell where the upscaling was performed using deep learning

168   (Figure S1). Rendering and 3D visualization of the whole segmented dataset revealed an intricate

169   network of DMVs embedded in an ER matrix. The majority of DMVs accumulated on the side of

170   the cell attached to the culture substrate (Figure 2B), although groups of DMVs were present

171   throughout the cell and always in contact with the ER network. Closer inspection showed that the

172   ER tubules with narrow luminal space linked several DMVs together, also connecting them to the

173 larger ER network (Figures 2C and 2D; Video S1). Therefore, we have named these structures

174 *ER connectors*.

175

176 **3D architecture of viral replication organelles provides insights into DMV biogenesis**

177 To gain insight into the biogenesis of the DMVs, we determined their 3D architecture by high-

178 resolution electron tomography analysis of SARS-CoV-2 infected Calu-3 cells. A total of 13

179 tomograms from uninfected cells and 7, 85 and 153 dual-tilt tomograms of cells fixed at 6, 12 and

180 24 h postinfection, respectively, were processed (Table S1; the complete data set is made

181 available for download on EMPIAR – ID 10490 and can be visualized through the MoBIE Fiji

182 plugin; see Figure S2A and Star Methods). For each tomogram, we identified and classified the

183 cellular and viral structures present (Table S1). This large dataset allowed us to identify different

184 topological compositions of the SARS-CoV-2 RO. Amongst all virus-induced structures, DMVs

185 were the most abundant. The average diameter, calculated at the DMVs' equator, was 291 ± 48

186 nm for the 24 h time point, in agreement with the results from TEM (Figure S2B and Figure 1G,

187 respectively). Smooth ER connectors were often found in close apposition to the DMVs' outer

188 membranes (Figures 3A-E). In some cases, DMVs were embedded into the rough ER such as the

189 DMV outer membrane was contiguous to the ER membrane, with several DMVs associated to

190 the same ER branch (Figures 3F and 3G, respectively; Video S2). This interconnection, together

191 with the presence of ribosomes on the DMVs' outer membrane (Figure S2C) suggests that DMVs

192 originate from the rough ER. Additionally, smooth ER connectors were seen linking DMVs to

193 the rough ER (Figures 3A-D and Figures 3H and 3I; Video S3), corroborating the observations

194 made by the FIB-SEM analysis. With very low frequency, we observed an opening in the DMV

195 membranes (Figure S2D) that connected the DMV interior to the cytosol. While the presence of

196 such openings could allow for the exchange of metabolites and for the release of newly

197 synthesized viral RNAs into the cytoplasm, their low frequency argues for a very short-lived

198 transition state prior to complete closure of the DMV membrane.

199 Consistent with recent reports (Klein et al., 2020; Ogando et al., 2020), DMV - DMV contacts

200 were also observed, either through funnel-like junctions between two DMVs (Figure S2E) or by

201 the formation of tabs and indentations in adjacent DMVs that resemble jigsaw puzzle pieces

202 (Figure S2F). Ultimately, these membrane bending events may generate fused DMVs (Figure
203 S2G) consisting of multiple vesicles sharing the same outer membrane, or multimembrane
204 vesicles formed by DMVs that have engulfed either a single or a double membrane vesicle
205 (Figure S2H).

206 Re-organization of the ER network was also confirmed by confocal microscopy of SARS-CoV-2
207 infected A549 lung epithelial cells overexpressing ACE2. We observed localization of the tubular
208 ER protein Reticulon 3 (RTN3) in the perinuclear region containing high amounts of double-
209 stranded RNA, a marker of viral replication, and the viral protein nsp3 (Figure 3J). Conversely,
210 the Sec61β subunit of the translocon was mostly excluded from this region, indicating that
211 despite the close link of DMVs to the ER, the synthesis of transmembrane or secreted proteins is
212 relocated to the vRO periphery (Figure 3J).

213 In our datasets, double membrane spherules, similar to the ones described for other coronaviruses
214 (Snijder et al., 2020), were only rarely seen in SARS-CoV-2 infected cells. These structures had a
215 diameter of ~75.5 ± 5.9 nm, an electron-dense interior and were linked to the connectors from
216 which they originated (Figures 3K and 3L; Video S4).

217 Altogether, our 3D reconstruction data provide strong evidence that SARS-CoV-2 reorganizes
218 the ER network and alters the morphology of this organelle to generate vROs, which consist
219 predominantly of DMVs, but also include other ER-derived structures such as ER connectors,
220 double membrane spherules and multi-membrane vesicles.

221

SARS-CoV-2 infection reorganizes peroxisomes, mitochondria and the secretory apparatus

223 In addition to the formation of *de novo* ER-derived organelles, SARS-CoV-2 replication alters
224 the morphology, the number and the function of several other cellular compartments. Of note, in
225 regions containing DMV clusters, we observed accumulation of peroxisomes in close proximity
226 to the DMVs' outer membrane (Figures 4A-C, Figures S3A and S3B; Video S5). These results
227 were confirmed by confocal microscopy and western blot analyses, showing a redistribution of
228 peroxisomes to dsRNA positive regions (Figures S3C and S3D) and an increase in the

229 peroxisome-associated protein PMP70 in infected cells (Figure S3E). Consistently, super-
230 resolution microscopy revealed an enclosing of the dsRNA signal by the peroxisomal signal
231 (Figure S3F), supporting the topology observed by electron tomography (Figures 4A-C). The
232 spatial proximity between peroxisomes and the sites of viral RNA replication (Figures S3A and
233 S3B) argues for a role of peroxisomes in the SARS-CoV-2 replication cycle such as the
234 prevention of oxidative damage to viral RNA or an involvement in lipid metabolism (Cook et al.,
235 2019) or a signaling platform mounting a cytokine response (Dixit et al., 2010).

236 Mitochondria were also altered in SARS-CoV-2 infected cells in several ways. First, they were
237 displaced and accumulated at the periphery of dsRNA positive regions (Figure S3G). Second,
238 mitochondria morphology was altered showing an increase of both intracristal space and matrix
239 density and conferring an electron-dense appearance in transmission electron microscopy (Figure
240 S3H). Third, in infected cells mitochondria were significantly thinner than in uninfected cells
241 (Figure S3I). Forth, in infected cells we observed a strong decrease in the total amounts of the
242 mitochondrial ATP synthase subunit 5B (ATP5B), a key factor for cellular energy production
243 (Figures S3J and S3K). Taken together, these results reveal strong perturbation of mitochondria
244 morphology and function, most likely reflecting SARS-CoV-2 induced impairment of cellular
245 energy metabolism.

246 The high frequency of budding events observed in the Golgi apparatus and the surrounding
247 vesicular membrane compartment indicates that these organelles provide membranes for SARS-
248 CoV-2 assembly (Figure 4D-F; Video S5). Within these cellular compartments, strings of viral
249 nucleoprotein, corresponding to dark-stained granules were found on bent membranes, which,
250 given the similarities in morphology to fully assembled virions, probably corresponding to the
251 early stages of virion budding (Figure S4A). Consistent with previous reports, we also observed
252 fully assembled virions with an average diameter of 80 ± 9.5 nm (Figure S4B) (Klein et al.,
253 2020). The global overview obtained from the large set of tomograms and the FIB-SEM data
254 reveal that assembly sites, corresponding to the Golgi and surrounding vesicles, and DMVs, the
255 RNA replication sites, are in close proximity, suggesting spatiotemporal coordination of the
256 different steps of the SARS-CoV-2 replication cycle (Figures 4A-F and Figure S1; Video S1 and
257 S5).

9

258 In uninfected cells, the secretory compartment showed well-defined morphology. The
259 polarization of the Golgi stacks allowed for reliable identification of the ER-to-Golgi
260 intermediate compartment (ERGIC) area and the presence of clathrin-coated vesicles marked the
261 *trans*-Golgi network (TGN) site (Figures S4C). Differently, fragmentation and dispersion of the
262 Golgi apparatus, with formation of multiple Golgi ministacks, was observed in SARS-CoV-2
263 infected cells as early as 6 h postinfection (Figures 4G and 4H and Figures S4D and S4E). While
264 fragmented Golgi cisternae were found in the vicinity of DMVs (Figures 4D-F, Figure S1) and
265 may constitute assembly sites, total Golgi area was only marginally reduced (Figure S4E),
266 suggesting that viral infection induced mainly a fragmentation and redistribution of the Golgi
267 cisternae (Figure S1). Due to the altered Golgi morphology, unambiguous identification of the
268 ERGIC and TGN sites is challenging in SARS-CoV-2 infected cells and therefore we use the
269 more general term vesicular-tubular compartment (VTC) when referring to the membranes in
270 close proximity of the ER and the Golgi stacks.

271 In addition to conventional assembly at the VTC and Golgi sites, assembly events were also
272 observed at electron-dense vesicles containing large numbers of virions (Figure S4F, panels i-iii).
273 Moreover, assembled virions were also present in multivesicular bodies (Figure S4F, iv). Such
274 structures could either provide an alternative secretory route or represent dead-end products of
275 the assembly process.

276

SARS-CoV-2 causes cytoskeleton remodeling important for viral replication

278 In addition to the secretory apparatus, mitochondria and peroxisomes, we also evaluated possible
279 cytoskeleton alterations in SARS-CoV-2-infected cells. To this end, we analyzed different classes
280 of cytoskeletal filaments, i.e. the microtubules, the actin microfilaments, and the intermediate
281 filaments by using A549-ACE2 cells that are superior to Calu-3 cells for light microscopy
282 imaging of these cellular elements. Consistent with a recent report (Bouhaddou et al., 2020), we
283 observed an accumulation of cortical actin at the plasma membrane of the infected cells,
284 suggesting a role for actin in virion release and/or virus spread (Figure 5A). Moreover, large
285 intracellular vesicles containing Spike and surrounded by an actin ring accumulated in SARS-
286 CoV-2 infected cells. In addition, SARS-CoV-2-infected cells exhibited a perinuclear inclusion

287 that stained positive for dsRNA and was surrounded by a cage of intermediate filaments (Figure

288 5A). This cage was surrounded by microtubules that were excluded from the dsRNA-containing

289 region (Figure 5A) arguing that intermediate filaments might serve to scaffold or confine the

290 vRO compartment. Interestingly, bundles of cytoskeletal filaments were also observed in

291 tomograms of infected Calu-3 cells in close proximity of the vROs (Figures S5A and S5B).

292 To better resolve the details of the intermediate filaments surrounding the vROs we performed

293 super-resolution STED microscopy on the whole cell volume (Figure 5B; Video S6). The dsRNA

294 region was seen mostly devoid of intermediate filaments, except for a few branches that

295 protruded within the vRO region (Figure 5B, panels iii). This arrangement suggests that

296 cytoskeletal elements might be displaced by clusters of DMVs, the main constituents of vROs, or

297 that the cytoskeleton, notably intermediate filaments support vRO formation.

298 To analyze the dynamics of intermediate filament remodeling in real time, we established a

299 SARS-CoV-2 reporter system (Pahmeier et al., 2020) in which a GFP, tagged with a nuclear

300 localization sequence (NLS), is anchored to the cytosolic side of the ER by the transmembrane

301 domain of Sec61β through a linker containing a recognition sequence for the SARS-CoV-2 main

302 protease 3-chymotrypsin-like (3CL) (Figure 5C, top panel). Upon infection by SARS-CoV-2, the

303 reporter protein is cleaved by 3CL, releasing the GFP-NLS moiety, which then translocates into

304 the nucleus. Thus, nuclear GFP signal serves as an identifier of SARS-CoV-2 infected cells. Co-

305 expression of fluorescently tagged vimentin together with this biosensor allowed for the

306 characterization of intermediate filaments remodeling and cage formation in infected cells by

307 means of live cell imaging (Figure 5C; Video S7). While spatial information was limited by the

308 resolution of our imaging system, which did not allow visualizing single intermediate filaments,

309 we were able to record the dynamics of cage formation. On average, nuclear translocation of the

310 reporter and vimentin cage formation became detectable at identical time frames, with the

311 majority of events being detected at 6.5 h postinfection (Figure 5D). A smaller proportion of GFP

312 translocation events, corresponding to viral spread, were observed at 16 h postinfection,

313 suggesting that a complete infection cycle might require ~9.5-10 h. At this late time point, a peak

314 in cell death, as judged by plasma membrane blebbing and cell disruption, was recorded, which

315 affected only ~20% of the cells. Therefore, the majority of infected cells were alive at 24 h

316 postinfection indicating that the phenotype we observed was not due to cell death.

11

317   To investigate the contribution of the different components of the cytoskeletal network to SARS-

318   CoV-2 replication, we treated infected cells with compounds altering cytoskeleton integrity and

319   dynamics (Figure 6A). For this we used drug concentrations that did not induce cytotoxicity as

320   determined by quantification of intracellular ATP levels (Figure 6B). We observed a robust

321   reduction in viral replication and amount of infectious virus released from cells that were treated

322   for 6 h with Withaferin A, a compound that disrupts the intermediate filaments network (Mohan

323   and Bargagna-Mohan, 2016) (Figures 6C and 6D), arguing for an important role for intermediate

324   filaments in vRO formation. Surprisingly, treatment with latrunculin A, a microfilament-

325   disrupting agent, did not affect viral replication or infectious particle production, suggesting a

326   limited contribution of the actin network to SARS-CoV-2 replication (Figures 6C and 6D).

327   Notably, while nocodazole and colcemid (inducing microtubule depolymerization) did not affect

328   SARS-CoV-2 replication, paclitaxel and vinblastine (inhibiting microtubule depolymerization or

329   polymerization, respectively), had a strong effect on the production of infectious extracellular

330   virus. These results reveal intermediate filaments and microtubules as critical host factors

331   contributing to SARS-CoV-2 replication and virus production, respectively.

332

DISCUSSION

334   In this study, we took advantage of several state-of-the-art imaging techniques to determine the

335   3D architecture and cytoplasmic configuration of SARS-CoV-2 ROs and virus-induced

336   alterations of cellular organelles. Consistent with very recent reports, we confirm that SARS-

337   CoV-2 alters the ER network to generate DMVs similar to other betacoronaviruses such as

338   SARS-CoV-1, MERS-CoV and MHV (Angelini et al., 2013; Hagemeijer et al., 2014; Knoops et

339   al., 2008; Snijder et al., 2020; Wolff et al., 2020). Importantly, several 3D volume EM datasets

340   acquired by FIB-SEM and the evaluation by 3D reconstruction of a full volume of an infected

341   cell shows that SARS-CoV-2 infection induces a massive spatial reorganization of the cytoplasm

342   to create a network of vROs. DMVs accumulate in the perinuclear region along with fragmented

343   and stacked membranes of the Golgi apparatus as well as peroxisomes. This replication-

344   conducive environment is enclosed by a cage-like structure consisting of intermediate filaments.

345   The DMVs were often interconnected or tethered by ER membranes, largely independent from

346   convoluted membranes that were reported for SARS-CoV-1 and MERS-CoV (Knoops et al.,

347 2008; Snijder et al., 2020). Instead, DMVs were often linked to stretched ER plates with a narrow

348 luminal space. These ER connectors are reminiscent of zippered ER reported for other

349 coronaviruses (Snijder et al., 2020). It is plausible that the lumen of the ER, from which DMVs

350 protrude, collapses, with ER membranes remaining connected to DMVs and getting stretched as

351 they grow over the course of infection. Alternatively, DMVs might first form at ER ends,

352 followed by collapse of the respective ER tubule.

353 With a lower frequency than DMVs, we could also detect double-membrane spherules that

354 exhibited a smaller diameter than the one of DMVs (~75 nm vs ~300 nm). These structures were

355 often located at the tip of the ER connectors and might result from connector membrane bending

356 and subsequent self-wrapping (Figures 3K and 3L). The absence of viral RNA with double-

357 membrane spherules (Snijder et al., 2020) suggests that these structures do not play a role in viral

358 RNA synthesis, but may instead constitute a defective by-product of vRO morphogenesis or exert

359 functions not detectable in *in vitro* cell culture systems.

360 Several reports have provided convincing evidence that MERS-CoV and SARS-CoV-1 RNA

361 synthesis occurs inside DMVs. Indeed, dsRNA as well as [^{3}H] uridine-labeled *de novo*

362 synthesized RNAs were detected inside DMVs by electron microscopy (Knoops et al., 2008;

363 Snijder et al., 2020). Moreover, very recently, viral RNA has been detected inside DMVs by

364 cryo-electron microscopy (Klein et al., 2020). Consistent with DMVs serving as sites of viral

365 RNA replication, proteinaceous pores have been reconstructed from MHV induced DMVs and

366 these pores most likely serve as sites for the exchange of metabolites, such as nucleoside

367 triphosphates, and exit of viral RNA into the cytoplasm (Wolff et al., 2020).

368 The mechanism underlying DMV biogenesis is poorly understood. Close examination of ~900

369 DMVs from more than 200 tomograms identified single openings in just a few of them (Figure

370 S2D; Table S1). While we cannot exclude that membrane integrity was compromised during

371 sample preparation, it is tempting to speculate that DMV openings might represent transition

372 states during DMV biogenesis prior to complete membrane closure. Of note, ribosomes were

373 occasionally detected on the cytosolic side of DMVs (Figure S2C), supporting a model in which

374 newly synthesized viral RNAs exiting DMVs are directly used for protein synthesis. Moreover,

375 the spatial organization of DMVs, ER and the secretory compartment as observed here allows an

376 optimal coordination between RNA synthesis, RNA translation and virion assembly. Indeed,

377 newly produced nucleocapsid proteins would already be properly localized to associate with

378 genomic RNA as it is exported from DMVs. These viral ribonucleoprotein particles would be

379 subsequently packaged and bud into the nearby VTC neighboring the DMVs. Supporting a tight

380 coordination between RNA replication/transcription and virus assembly, small stacks of

381 fragmented Golgi-like membranes, which contained virions, were often found in the vicinity of

382 DMVs (Figure 4; Figure S1 and Figures S4D and S4E).

383 Juxtaposed to DMVs we observed the accumulation of peroxisomes, which were also more

384 abundant in SARS-CoV-2-infected cells than in control cells (Figures S3A-F). These organelles

385 might contribute to viral replication e.g. by reducing oxidative stress that might result from the

386 extensive remodeling of cellular endomembranes by SARS-CoV-2, or by providing additional

387 lipids required for DMV formation (Cook et al., 2019). Finally, the translocon subunit Sec61β, an

388 abundant ER protein, was mostly excluded from the vRO compartment (Figure 3J) strongly

389 suggesting a partitioning of ER functions in infected cells. Consistently, our confocal microscopy

390 analysis of infected cells revealed that the ER-bending protein RTN3 was enriched in the

391 perinuclear region where dsRNA accumulated, arguing that SARS-CoV-2 might hijack distinct

392 ER-shaping proteins for vRO biogenesis. Such host cell factor usurpation has been reported for

393 other RNA viruses. For instance, the ER-shaping proteins atlastin 2, RTN3 and the reticulophagy

394 factor FAM134B were recently shown to be involved in the biogenesis of flavivirus replication

395 organelles (Lennemann and Coyne, 2017; Monel et al., 2019; Neufeldt et al., 2019). It is tempting

396 to speculate that the functions of such host factors might be regulated by nsp3-4 shown for other

397 coronaviruses to be sufficient to induce DMVs (Angelini et al., 2013; Hagemeijer et al., 2014).

398 Apart from the ER and peroxisomes, several other cellular organelles were found to be remodeled

399 in SARS-CoV-2 infected cells. This includes mitochondria displaying swollen cristae and matrix

400 condensation, along with reduced components of the ATP synthase. This observation is

401 consistent with transcriptional changes reported for SARS-CoV-2 infected cells indicating

402 reduced oxidative phosphorylation and pointing towards metabolic reprogramming triggered by

403 the virus (Neufeldt et al., 2020).

404 Nocodazole and colcemid induce microtubule depolymerisation and did not affect SARS-CoV-2

405 replication (Figures 6C and 6D), whereas alteration of microtubule dynamics, either by inhibiting

406 polymerization or depolymerization of the microtubular network, strongly suppressed the

407   production of infectious SARS-CoV-2 (Figure 6D). Paclitaxel induces microtubule bundles that

408   associate with Golgi fragments (Sandoval et al., 1984; Wehland et al., 1983). This might prevent

409   redistribution of Golgi ministacks close to the viral replication sites, the DMVs, thus altering the

410   spatio-temporal coordination of viral replication and assembly. Although other mechanisms

411   might account for the observed phenotype, microtubules play an important role in shaping Golgi

412   structure and function, arguing that the observed reduction in extracellular infectivity is linked to

413   alteration of the assembly or secretion of virus particles at the Golgi. In contrast, disruption of the

414   actin microfilament network with latrunculin A did not affect virus production and spread.

415   Nevertheless, in infected cells we observed a striking redistribution of cortical actin. This might

416   reflect the formation of filopodia suggested to allow rapid spread of SARS-CoV-2 in infected

417   tissues (Bouhaddou et al., 2020).

418   DMVs concentrate within a cage-like structure, which is induced upon infection and composed of

419   intermediate filaments that might aid in spatial segregation of DMVs in the perinuclear area. It is

420   unknown whether such structures are shared by other coronaviruses, but it is reminiscent of those

421   we have previously reported for Zika virus (Cortese et al., 2017), a positive-strand RNA virus

422   belonging to the *Flaviviridae* family. Live cell imaging and super-resolution microscopy with

423   SARS-CoV-2 infected cells highlighted virus-induced alteration of the vimentin network (Figure

424   5B and 5C; Videos S6 and S7). Consistently, enforced pharmacological aggregation of

425   intermediate filaments with Withaferin A was detrimental for viral replication supporting that this

426   structure contributes to viral replication (Figure 6C). Of note, a recent systems biology study

427   revealed that the phosphorylation levels of serine residues 39 and 56 of vimentin are decreased in

428   SARS-CoV-2-infected cells (Bouhaddou et al., 2020), and phosphorylation of serine residue 39

429   has been shown to impede intermediate filament polymerization (Eriksson et al., 2004). In

430   addition, SARS-CoV-2 nsp7 associates with the RhoA kinase of the Rho/Rac/Cdc42 pathway,

431   which positively regulates PAK1/2-dependent phosphorylation of vimentin (Gordon et al., 2020).

432   Altogether, these data provide compelling evidence that SARS-CoV-2 regulates the dynamics of

433   intermediate filaments in infected cells, possibly through the modulation of posttranslational

434   modifications. Whether nsp7 is responsible for the observed changes in intermediate filament

435   dynamics and cage formation remains to be determined.

436   Intermediate filaments also play an important role in innate immunity and induction of a cellular

437   antiviral state (Mostowy and Shenoy, 2015). Interestingly, type I interferon treatment was shown

438 to alter the integrity of arterivirus nsp2/3-induced DMVs (Oudshoorn et al., 2016). This raises the

439 hypothesis that the SARS-CoV-2-induced vimentin cage might reduce access of the viral

440 replication compartment to sensors of the cellular innate defense system. Moreover, the sub-

441 population of vimentin located at the cell surface was shown to contribute to SARS-CoV-2 S-

442 mediated cell entry of virus-like particles (Yu et al., 2016). While such participation in the entry

443 of genuine virus particles was not investigated, the redistribution of intermediate filaments

444 around the replication compartment and its expected exclusion from the plasma membrane would

445 constitute a mechanism to avoid super-infection or retention of newly synthesized virions at the

446 surface of the virus-producing cells.

447 In conclusion, this study reports a comprehensive overview of SARS-CoV-2 induced vROs and

448 virus-induced alterations of cellular organelles. We employed an integrative imaging analysis and

449 generated an unprecedented repository of 3D structure information of virus-induced substructures

450 and whole cell volumes, deduced from a FIB-SEM dataset and around 250 tomograms. All these

451 data will be shared with the scientific community for download through the EMPIAR platform

452 and for smooth online visualization through MoBIE (Vergara et al., 2020). This data-rich

453 resource will support the global investigative effort to study how SARS-CoV-2 interacts with its

454 host and become an important tool to unveil novel antiviral targets for the development of host-

455 targeting drugs suppressing viral replication as well as virus-induced cell damage.

456

457 **LIMITATIONS OF THE STUDY**

458 Our study describes morphological changes induced by SARS-CoV-2 in the host cell. Although

459 we used a human lung-derived cell line that can be used as respiratory model, it remains to be

460 determined how well observed cellular alterations reflect those induced in vivo. Moreover, there

461 are still several open questions regarding the molecular mechanisms responsible for the observed

462 perturbations. For instance, the biogenesis of SARS-CoV-2 ROs is still poorly characterized and

463 we do not have detailed information on the host or viral factors that contribute to RO formation.

464 Identification of these factors can provide promising candidates for developing compounds that

465 could limit viral replication. Likewise, further investigation is required to determine the

466 molecular mechanisms underlying cellular organelle reshaping induced by SARS-CoV-2

467 infection, such as Golgi fragmentation or cytoskeletal remodeling as well as the association

468   between peroxisomes and viral DMVs. Using our ultrastructural data set as a foundation, we can

469   begin to design studies aimed at answering these questions that will provide useful insights into

470   SARS-CoV-2 pathogenies and will allow us to better understand the interplay between the virus

471   and the host cell.

Acknowledgments

Author Contributions

Project design: M.C., Y.S., R.B.; EM sample preparation: V.M.J.O., N.L.S. and M.C.; performance of TEM experiments: V.M.J.O. and Y.S.; TEM tomography acquisition: S.K. and M.B.; FIB-SEM acquisition: N.L.S and P.R. with support from K.M., R.M.T., M.S.B. and R.S.M.; design of the FIB-SEM data image analysis: J.H.; image analysis on TEM tomography and FIB-SEM data: S.K., P.R., Y.S., G.M., V.M.J.O., V.G., M.B., K.M., I.R.B., R.S.M., N.L.S., M.S.B., Y.S.; editing of 3D movies: G.M., J.H., J.L.; implementation of image visualization tools for TEM tomography and FIB-SEM data: M.S., C.P., C.T.; live-cell imaging: A.R.; image analysis light microscopy: J.L., J.F., M.C.; investigation: M.C., B.C., C.J.N., N.H.; STED acquisition and analysis: V.L.; manuscript writing: M.C., C.J.N., R.B., L.C.C.; resources: Y.S., S.B., M.S.; Data visualization: M.C., A.R., J.H.; Project supervision: Y.S., R.B.; Funding: Y.S., R.B.

Declaration of Interests

The authors declare no competing interests.

Figure Legends

Figure 1. SARS-CoV2 infection kinetics in pulmonary epithelial cells.

(A) Time course of SARS-CoV-2 replication in infected Calu-3 cells (MOI = 5) as detected by immunofluorescence using a dsRNA antibody (white). Nuclear DNA was stained with DAPI (blue). Scale bar: 40 μm. (B) Percentage of dsRNA positive cells quantified from panel (A). (C and D) Intra- and extracellular viral RNA levels measured by RT-qPCR. (E) Extracellular infectivity measured by plaque assay. Means and SDs of three independent experiments are shown in panels B-E. (F) Transmission electron microscopy images of 70-nm-thin sections of resin-embedded Calu-3 cells infected with SARS-CoV-2 (MOI = 5) and imaged at the indicated time points after infection. DMVs, double membrane vesicles; C, connectors; LD, lipid droplet; Gg, glycogen granules; orange arrow heads, completed virions; yellow arrowhead, budding virion. Areas in yellow rectangles are magnified in the corresponding panels marked with roman letters. Red dotted lines indicate regions with accumulations of DMVs. (G) Relative frequency distribution of DMV diameters determined at the different time points after infection. Gaussian fits are shown as overlay. N = 43, 40 and 48 DMVs for 6 h, 12 h and 48 h postinfection, respectively.

Figure 2. FIB-SEM analysis of whole cell volume of a SARS-CoV-2 infected cell reveals a network of DMVs and ER.

Calu-3 cells were infected with SARS-CoV-2 (MOI = 5) for 24 h before being fixed and prepared for FIB-SEM analysis. (A) Two different slices through the cell volume. Note the tight association of the infected cell in the middle with the neighboring cells, giving the infected cell an hourglass-like shape in the top panel. (B) 3D rendering of the infected cell. The color code of subcellular structures is depicted on the bottom of the figure. (C) Zoom-in of the area indicated with rectangle in (B) showing a cluster of DMVs. (D) Detail of DMV - ER connections (i). DMVs are shown in red, membrane connectors are shown in citrus. (ii) Same as in (i) but with high level transparencies for DMVs and ER regions, except the areas in contact with the ER connectors. (iii and iv) Two orthogonal slices showing the raw data of the same region of the respective left panel. Scale bars: 2 μm in panels A and B, 500 nm in panels C and D. See also Figure S1 and Video S1.

Figure 3. High-resolution analysis of ER - DMV inter-connectivity and selective recruitment of ER-resident proteins to sites of viral replication organelles.

Electron tomography and 3D rendering of SARS-CoV-2 infected Calu-3 cells (MOI = 5) harvested 12 h after infection. (A) Slice through the tomogram. (B) Same region as in (A) with superimposed rendering of cellular and viral organelles. The color code of visualized structures for this and subsequent panels is given in the lower left of the figure. (C) 3D reconstruction of the area indicated with yellow rectangle in (B). (D) Magnified view of DMVs (red) in close contact

19

542 with membrane connectors (citrus). (E) Magnified view of a DMV in close contact with the ER
543 (green). An ER connector forming a hook is also visible (bottom right). (F) Consecutive slices of
544 a tomogram depicting two adjacent DMVs sharing the outer-membrane with the ER. (G) Side
545 view of the 3D rendering. (H) Orthogonal slices of a tomogram depicting a membrane connector
546 in contact with a DMV and with the ER. A superposition of rendered DMV and ER is shown in
547 the right panel. (I) 3D rendering view of the DMV and its connectivity to the ER. Scale bars in all
548 panels: 200 nm. (J) A549-ACE2 cells were infected with SARS-CoV-2 for 16 h, fixed and
549 stained with primary antibodies of the given specificities. DNA was stained with DAPI (blue).
550 Single slices through deconvoluted z-stacks are shown. Scale bar, 10 μm. (K) Consecutive slices
551 and (L) 3D rendering of membrane connector bending to form a double membrane spherule. Red
552 arrows point to double membrane spherules. Scale bars: 200 nm. See also Figure S2 and Video
553 S2, S3, and S4.

554

**Figure 4. Spatial coupling of SARS-CoV-2 replication and assembly sites mediated by close
proximity of DMVs, vesicular-tubular compartment and Golgi apparatus**

557 (A-F) Electron tomography and 3D rendering of SARS-CoV-2 infected Calu-3 cells (MOI = 0.5)
558 harvested 24 h after infection. (A) Slice through the tomogram. (B) Same region as in (A) with
559 superimposed rendering of cellular and viral organelles that are specified on the bottom of the
560 figure. (C) 3D rendering of organelles visualized in (A). (D-F) Zoom on the vesicular-tubular
561 compartment (VTC; cyan) and Golgi apparatus (dark blue) with budding virions (yellow) and
562 fully assembled virions (orange). Scale bars: 200 nm. (G) Time course of Golgi fragmentation in
563 SARS-CoV-2 (MOI = 5) infected A549-ACE2 cells. Asterisks indicate infected cells. Scale bar,
564 10 μm. (H) Quantification of images in (G). For each cell, the largest Golgi fragment was
565 calculated. Each dot indicates the mean values from at least 30 individual cells. Mean and SD of
566 triplicate experiments are shown. P-value was calculated with Student's t-test. ** = p<0.01.See
567 also Figures S1, S2 and S4 and Video S5.

568

**Figure 5. A network of intermediate filaments surrounds SARS-CoV2 replication
organelles.**

571 (A) A549-ACE2 cells were infected with SARS-CoV-2 for 16 h (MOI = 5), fixed and stained
572 with antibodies of the given specificities. DNA was stained with DAPI (blue). A single slice
573 through a deconvolved z-stack is shown. The regions in the yellow boxes are magnified in the
574 zoom panels on the left. Scale bar, 10 μm. (B) Cells infected as in (A) were fixed and stained
575 with antibodies directed against dsRNA, the viral replication intermediate, and vimentin. Images
576 were taken using an Abberior instruments STED microscope. Z-stacks comprising whole cells
577 were acquired. Selected slices through the stack are shown in (i). A central slice with dsRNA
578 (green) and vimentin (gray) signals is shown in (ii). The region in the yellow box is magnified in
579 panels (iii). A 3D rendered model of the dsRNA (green) and vimentin (red) signals is shown in
580 panel (iv). (C) Live cell imaging of SARS-CoV-2 infected A549-ACE2 cells transiently
581 expressing an mCherry-tagged vimentin protein (magenta) and a GFP-NSL-tagged SARS-CoV-2
582 fluorescent reporter (the structure of this reporter is given on the top). Infected cells show nuclear

583 translocation of the GFP-NLS reporter. Scale bar, 20 μm. NLS, nuclear localization sequence;
584 GFP, green fluorescent protein; TM, transmembrane region of Sec61β; black arrowhead, SARS-
585 CoV-2 3C-like protease cleavage site. (D) Frequency distribution of the GFP-NLS nuclear
586 translocation (green bars), vimentin peri-nuclear accumulation (red bars) and infected cell death
587 (gray bars) events. Gaussian fit of each dataset is shown. See also Figure S5 and Videos S6 and
588 S7.

589

590 **Figure 6. Important role of the cytoskeleton for productive SARS-CoV-2 replication and**
591 **virus particle production.**

592 (A) Compounds that alter the cytoskeletal network were tested on Vero E6 cells infected with
593 SARS-CoV-2. Infection was allowed to proceed for 2 h prior to addition of given concentrations
594 of the indicated compounds. Cells were fixed at 8 h postinfection and dsRNA as well as the
595 indicated cytoskeleton elements were detected by immunofluorescence microscopy using specific
596 antibodies. (B) Cell viability after 6 h treatment with the indicated compounds as determined by
597 quantification of intracellular ATP levels. (C) Percentage of infected cells as determined by
598 dsRNA staining of cells treated as in (A). (D) Amounts of infectious SARS-CoV-2 released into
599 the culture supernatant of cells treated as in (A) was quantified by using plaque assay. Panels (C)
600 and (D) show means and SDs; each dot represents the mean of technical triplicates (C) or
601 duplicates (D).

602

STAR METHODS

RESOURCE AVAILABILITY

Lead Contact

Further information and requests for resources and reagents should be directed to and will be fulfilled by the lead contact, Ralf Bartenschlager (ralf.bartenschlager@med.uni-heidelberg.de).

Materials Availability

Plasmids and/or cell lines will be distributed under the terms of a material transfer agreement.

Data and Code Availability

The tomograms and FIB-SEM datasets generated during this study are available at EMPIAR (ID 10490). Links to the individual tomograms are available in supplemental Table S1. Additional Supplemental Items are available from Mendeley Data at http://dx.doi.org/10.17632/8fc7fr8g63.1.

EXPERIMENTAL MODELS AND SUBJECT DETAILS

Cell lines

VeroE6, A549 and HEK293T cells were obtained from ATCC and grown in complete Dulbecco's modified Eagle medium (DMEM) containing 10% fetal calf serum (FCS), 2 mM L-glutamine, non-essential amino acids, 100 U/ml penicillin and 100 µg/ml streptomycin. Calu-3 cells (a kind gift from Dr. Manfred Frey, Mannheim) were grown in complete DMEM with a final concentration of 20% FCS and supplemented with 10 mM sodium pyruvate. A549 cells stably expressing ACE2 (A549-ACE2) were generated as described recently (Klein et al., 2020).

Viruses

624 The SARS-CoV-2 isolate Bavpat1/2020 was obtained by the European Virology Archive (Ref-

625 SKU: 026V-03883) at passage 2. Working virus stocks were generated by passaging the virus

626 two times in VeroE6 cells.

METHOD DETAILS

Light microscopy (confocal and STED)

629 For light microscopy Calu-3 cells or A549-ACE2 cells were seeded onto glass coverslips one day

630 prior to infection with SARS-CoV-2. Samples were fixed with 4% paraformaldehyde buffered in

631 PBS for 30 min at room temperature (RT). Plates containing the coverslips were submerged in

632 6% formaldehyde for 30 min at RT before being transported outside the biosafety level 3 (BSL3)

633 area. Samples were then washed in PBS, permeabilized with 0.1% Triton-X100 in PBS for 10

634 min at RT, blocked with 5% milk in PBST (PBS with 0.01% Tween-20) for 1 h and incubated

635 with primary antibodies for an additional hour at RT in 5% milk-PBST blocking buffer. Samples

636 were washed 3 times in PBST and incubated with Alexa-fluor conjugated secondary antibodies

637 for 45 min at RT in PBST. Samples were washed 3 times in PBST, twice in PBS and mounted

638 with Fluoromount-G mounting medium containing DAPI (Southern Biotechnology). Imaging

639 was performed using a 63x oil immersion objective (NA, 1.4; Leica APO CS2) on a Leica SP8

640 system with lighting configuration.

641 Primary antibodies used in this study were: J2 mouse anti-dsRNA (Scicons, # 10010500); mouse

642 anti-SARS-CoV-2 Nucleocapsid (Sino Biological, # 40143-MM05); mouse anti-SARS-CoV

643 spike (Genetex, GTX632604-100), mouse anti-RTN3 (Santa-Cruz, #sc-374599), rabbit anti-

644 PMP70 (abcam, ab3421), rabbit anti-GM130 (cell signaling, #12480), sheep anti-TGN46 (biorad,

645 AHP500G) , mouse anti-tubulin (ThermoFischer, # MA5-17193), rabbit anti-vimentin (abcam,

646 #ab188499). For actin staining, 565-ATTO conjugated phalloidin was diluted in 500 µl of

647   methanol according to the manufacturer's instructions (Sigma, #94072) and added together with

648   the secondary antibodies. Alexa Fluor 488, 568 and 647 fluorescent-dye conjugated secondary

649   antibodies were used in this study.

650   For stimulated emission depletion (STED) microscopy, samples were prepared as described

651   above except that high-precision coverslips were used (Marienfeld, # 0117520) and secondary

652   antibodies were conjugated either with STAR-RED, ATTO-590 or ATTO-594. Dual-color 2D

653   stimulated emission depletion (STED) microscopy was performed on an Expert Line STED

654   system (Abberior Instruments GmbH, Göttingen, Germany), using a 100x oil immersion

655   objective (NA, 1.4; Olympus UPlanSApo) and excitation with the 590- and 640-nm laser lines.

656   775 nm STED laser (15% of the maximal power of 3 mW) was used for depletion with pixel

657   dwell time of 10 to 15 μs and 15-nm xy sampling. For 3D STED data, 40% of the STED laser

658   power was used for fluorescence depletion in the Z-axis and DyMIN illumination scheme was

659   used to minimize bleaching. Sampling frequency was 30 nm in xy and 70 nm in z axis (xyz).

660   STED images were restored with Huygens Deconvolution (Scientific Volume Imaging) using

661   Classic Maximum Likelihood Estimation (CMLE) algorithm and Deconvolution Express mode

662   with Conservative settings. The 3D rendering and the movie of the vimentin staining were

663   generated in IMARIS v8.0 (Oxford instruments).

664   **Live cell imaging**

665   The SARS-CoV-2 reporter construct used for live cell imaging will be described in detail

666   elsewhere (Pahmeier et al., 2020). In brief, it is an engineered fusion protein composed of (from

667   N- to C-terminus) green fluorescence protein, the nuclear localization sequence from simian virus

668   40, a linker sequence containing the consensus cleavage site of the 3CL protease of SARS-CoV-

669   1, and the transmembrane region of Sec61β. Lentiviruses encoding SARS-CoV-2 reporter and

670   mCherry-tagged vimentin were generated transfecting HEK293T cells with pWPI-RC_CoV-2

24

671 and pWPI-mCherryVimentin, respectively, and with helper plasmids pMD2-VSV-G and pCMV-

672 Gag-Pol (gift from Dieder Trono). After 48 h post-transfection, supernatants containing

673 lentiviruses were harvested and filtered through a 0.45 µm filter and stored at -80°C. For live cell

674 imaging, A549-ACE2 cells were transduced with lentiviruses encoding for the SARS-CoV-2

675 reporter and a mCherry-tagged vimentin and seeded onto 35 mm diameter dishes with polymer

676 coated bottom and sealable lid (ibidi, # 81156). 16 h post-transduction, cells were infected with

677 SARS-CoV-2 (MOI=5) in growth medium without phenol-red. The lid was locked and sealed

678 with silicon to prevent evaporation. 3 h after infection, imaging of cells was started using a Nikon

679 Eclipse Ti inverted microscope, equipped with a 20x objective. Multiple fields were defined and

680 image acquisition was performed at intervals of 10 min for 24 h by using the automated Nikon

681 perfect focus system. Images were analyzed with the Nikon NIS Element Advanced Research

682 program.

683 **Plaque assay**

684 Plaque assay was performed as previously described (Klein et al., 2020). Briefly, VeroE6 cells

685 seeded in duplicate wells were inoculated with serial 10-fold dilutions of SARS-CoV-2

686 containing supernatants for 1 h at 37°C. One hour later, the inoculum was replaced by serum-free

687 MEM (Gibco, Life Technologies) containing 0.8% carboxymethylcellulose (Sigma-Aldrich).

688 Samples were fixed three days postinfection with formaldehyde, directly added to the medium to

689 a final concentration of 5% for 30 min. Plates were plunged in 6% formaldehyde for inactivation

690 and transported outside the BSL3 area. Plates were then washed extensively with water before

691 being stained with 1% crystal violet and 10% ethanol for 30 min. Plates were rinsed with water,

692 the number of plaques was counted and virus titers were calculated.

693 **Cytotoxicity Measurement**

694   VeroE6 cells were seeded into 96-well plates at a confluency of 7E+03 cells per well and treated

695   for 6 h with serial 2-fold dilutions of the different compounds. For latrunculinA, the highest used

696   concentration was 5 µM, for all the other compounds a starting concentration of 50 µM was used.

697   Nocodazole, paclitaxel and vinblastine were purchased from Sigma. LatrunculinA was obtained

698   from Santa Cruz Biotechnology. WithaferinA was obtained from Abcam. DMSO was used as

699   control. Cell viability was determined by quantitation of ATP concentration using the CellTiter-

700   Glo assay (Promega) as recommended by the manufacturer. A Mithras LB 940 plate reader

701   (Berthold Industries) was used to measure the luminescence. A compound concentration that

702   reduced the ATP amounts more than 20% was considered cytotoxic.

703   **Drug treatments**

704   VeroE6 cells were seeded in triplicates at a confluency of 7E+03 cells per well in black-wall

705   glass-bottom 96 well plates (Corning, # 353219). Cells were infected with SARS-CoV-2

706   (MOI=5) for 1 h at 37°C. At 2 h postinfection, virus inoculum was removed, cells were washed

707   with PBS and media containing different concentrations of the compounds were added to the

708   cells. DMSO was used as control. 8 h postinfection, virus supernatants were harvested and used

709   for plaque assay. Infected cells were washed in PBS, fixed in 6% formaldehyde, processed for

710   immunofluorescence as described above and imaged as previously reported (Pape et al., 2020).

711   **RT-qPCR**

712   Total RNA was isolated with the Nucleospin RNA extraction kit (Macherey-Nagel) according to

713   the manufacturer's instructions. A high capacity cDNA reverse transcription kit (ThermoFisher)

714   was used for cDNA synthesis from that total RNA. cDNA samples were diluted 1:15 and used for

715   qPCR with the iTaq Universal SYBR green mastermix (Biorad). Primers used in this study were:

716   SARS-CoV-2-N (forward) 5'-GCCTCTTCTCGTTCCTCATCAC-3', SARS-CoV-2-N (reverse)

717   5'-AGCAGCATCACCGCCATTG-3', HPRT (forward) 5'-CCTGGCGTCGTGATTAGTG-3'

718 and HPRT (reverse) 5'-ACACCCTTTCCAAATCCTCAG-3'. Relative abundance of each

719 specific RNA was determined by correcting the cycle threshold values for the PCR efficiency of

720 each primer set and normalizing to the hypoxanthine phosphoribosyltransferase 1 (HPRT)

721 transcript levels.

Sample processing for TEM

723 Calu-3 cells grown on glass coverslips were infected with SARS-CoV-2 either at MOI=5 or

724 MOI=0.5 as specified in the results section. Cells were fixed by adding 2x concentrated EM

725 fixative (composition of the 1x fixative: 2.5% glutaraldehyde in 50 mM Na-cacodylate buffer

726 (pH 7.4) containing 50 mM KCl, 2.6 mM $MgCl_2$, 2.6 mM $CaCl_2$ and 2% sucrose) to the cell

727 culture medium (1:1) for 5 min at RT in 12 wells plates. Fixative was removed and replaced by

728 1x fixative for 2 h at RT. Plates were plunged in 6% formaldehyde for inactivation for 30 min at

729 RT before being transported outside the BSL3 area. Fixative was exchanged again with 1x EM

730 fixative and the samples were stored at 4°C until further processing. Prior to embedding cells

731 were rinsed 6 times with 100 mM Na-cacodylate for 10 min each. Subsequently, cells were post-

732 fixed with osmium-ferricyanide (1% OsO_4, 1.5% $K_3Fe(III)(CN)_6$, 0.065 M Na-cacodylate buffer)

733 for 2 h at 4°C in the dark. Further processing was done in the microwave. Cells were washed with

734 dH_2O 5x for 1 min each, stained with 1% uranyl acetate in dH_2O 4x for 2 min each, rinsed 3x

735 with dH_2O for 1 min. Dehydration with an ethanol series (50%, 70%, 90% and 4x 100%) was

736 then performed for 40 sec each on ice in the microwave. Cells were infiltrated in Epon 812 resin

737 with increasing percentages of this resin in ethanol (10%, 30%, 50%, 70%, 90% and 2x 100%)

738 for 3 min each in the microwave. The coverslips with the cells facing down were placed on a

739 BEEM capsule filled with Epon 812 resin. Beem capsule and coverslip were turned upside down

740 and polymerized at 60°C. After one day the glass coverslips were removed from the blocks that

741 were incubated for 2 more days at 60°C. Ultrathin sections (70 nm) were obtained with a UC7

742   Leica conventional ultramicrotome with a diamond knife (Diatome) and collected on slot grids.

743   Grids were post-stained with Uranyl acetate and lead citrate. Sections were analyzed with a JEOL

744   2010 plus transmission electron microscope equipped with a Matataki sCMOS camera.

745   **Electron tomography (sample acquisition, reconstruction and rendering)**

746   Sections of 300 nm (Calu-3 cells, MOI=0.5, 24 h postinfection) and 200 nm (all other conditions)

747   thickness processed as described for TEM, were collected on Formvar-coated slot grids. After

748   post-staining, screening images were acquired at 1000× and 3000× magnification at points evenly

749   distributed across one section. This was done using advanced SerialEM functionality at a JEM

750   2100 Plus electron microscope (JEOL Ltd., Akishima, Japan) equipped with a Jeol Matataki

751   sCMOS camera (Schorb et al., 2019). The higher magnification images were manually screened

752   for target features. After transferring and registering the grids to a TF30 microscope (Thermo

753   Fisher Scientific, Waltham, MA, USA), equipped with a Gatan OneView (Gatan, Inc. Pleasanton,

754   US), precise target positions were manually selected within the previously defined regions and

755   acquired by dual axis tomography (-60° to +60° per axis; increment: 1°) at 15,500× magnification

756   (1.55 nm/px). The tilt series were reconstructed on a high-performance computer cluster using

757   IMOD's automated batch reconstruction (Kremer et al., 1996; Mastronarde, 2005; Mastronarde

758   and Held, 2017). Selected tomograms or parts thereof were manually segmented in Amira-Avizo

759   software Version 2020.1, using the magic wand and the brush segmentation tools. Volume

760   rendering and animations were computed with Amira and post-processed in ImageJ (Schindelin

761   et al., 2012; Schneider et al., 2012).

762   **Sample preparation for FIB-SEM**

763   Calu-3 cells were grown on 35 mm diameter MatTek dishes with glass bottom and were prepared

764   (infection and fixation) as described above for TEM. Extra post-staining steps were performed

765   (the so called OTO post-staining). Cells were post-fixed with osmium-ferricyanide (1% OsO_4,

766 1.5% $K_3Fe(III)(CN)_6$, 0.065 M Na-cacodylate buffer) for 2h at 4°C in the dark. Further

767 processing was done in the microwave. Cells were rinsed 5x in dH_2O for 1 min and treated with

768 1% thiocarbohydrazide in dH_2O 4x for 2 min each. Cells were rinse 3x with dH_2O for 1 min and

769 stained 4x with 2% osmium tetroxide in dH_2O 4x for 2 min each. Cells were rinsed 3x with dH_2O

770 for 1 min, stained with 1% Uranyl acetate in dH_2O 4x for 2 min each. Dehydration and

771 embedding were done as described for TEM sample preparation except that Durcupan resin was

772 used. Cells were embedded in a thin layer of Durcupan resin covered with a coverslip and

773 polymerized overnight at 60°C. After one day the resin slab was detached from the coverslips,

774 polymerized at 100°C for a few hours and at 60°C overnight. The polymerized samples were

775 mounted on SEM stubs.

776 **FIB-SEM**

777 FIB-SEM image acquisition was performed with a Zeiss Crossbeam 540 or a Zeiss Crossbeam

778 550, using the Atlas5 software (FIBICs, Carl Zeiss Microscopy). Briefly, a platinum coating was

779 deposited over the cells of interest and autotune marks were etched and used for post-acquisition

780 image alignment. The imaging surface was exposed by FIB-milling of a 25-30 µm deep trench.

781 FIB slicing during the run was obtained at 700 pA/1.5 nA. All datasets were acquired at 1.5 kV

782 and 700 pA current using an energy-selective back-scattered electron detector (ESB). The cells

783 were acquired at 8x8x8 nm (or $5\times5\times5$ nm) voxel size.

784 Alignment of image slices was performed by a workflow based on Alignment to Median

785 Smoothed Template (AMST) (Hennies et al., 2020). Pre-alignment was performed by linear stack

786 alignment with SIFT (Lowe, 2004) and subsequent template matching on the autotune marks.

787 The displacements obtained by template matching were smoothed along the z-direction for more

788 robustness and applied to the SIFT aligned data stack. Subsequent AMST yielded the final

789 aligned datasets.

790 Segmentation of DMVs, ER and mitochondria was performed in semi- and fully-automated

791 manner in an original workflow that will be detailed elsewhere. The semi-automated workflow,

792 based on supervoxel merging using Paintera (https://github.com/saalfeldlab/paintera)

793 (Hanslovsky et al., 2020), was used to obtain the necessary ground truth for the automated

794 workflow. The automated segmentation is an adaptation of the multicut pipeline (Beier et al.,

795 2017), optimized for the segmentation of cellular organelles. Masks for the target cells were

796 obtained using Microscopy Image Browser MIB (Belevich et al., 2016) by annotation of selected

797 slices and interpolation. Nuclei were segmented in MIB using the graph-cut approach. Golgi

798 stacks were segmented using MIB by annotation of selected slices with interpolation. Subsequent

799 adaptive thresholding (Otsu, 1979) within the annotated area, individually for each Golgi stack,

800 yielded the final segmentation. For the mock cell, we annotated ~20 stacks and used a U-Net

801 (Çiçek et al., 2016) to scale up to the full cell. 3D renderings of above described segmentations

802 were performed using Drishti (Limaye, 2012).

803 **Electron microscopy dataset visualization through MoBIE**

804 The Fiji plugin MoBIE can be used to visualize all the tomographic datasets (Vergara et al.,

805 2020). Instructions for the plugin download and installation can be found at the following link:

806 https://github.com/mobie/mobie-viewer-fiji. To visualize the electron microscopy datasets, the

807 link to the datasets (https://github.com/mobie/covid-tomo-datasets for the tomograms and

808 https://github.com/mobie/covid-em-datasets for the FIB-SEM datasets) should be inserted into

809 the "Project location" of Fiji. Additional information how to access and used the datasets is

810 provided in Table S1.

811 **STATISTICAL ANALYSIS AND QUANTIFICATION**

812   All statistical analyses were performed with the GraphPad Prism 7.04 software package (LaJolla,

813   CA, USA). Data sets were considered significantly different if the P-value was less than 0.05. For

814   each experiment, the performed statistical analysis and the sample sizes are given in the

815   respective figure legend.

816

Supplemental Information

Table S1. List of tomograms and annotations. Related to Figures 2, 3 and 4

Video S1. FIB-SEM analysis of a SARS-CoV-2 infected cell. Related to Figure 2

Video S2. Electron tomogram of DMVs and their connection with the ER. Related to Figure 3

Video S3. Electron tomogram of DMVs in contact with ER connectors. Related to Figure 3

Video S4. Electron tomogram of double-membrane spherules and their association with the ER. Related to Figure 3

Video S5. Electron tomogram of SARS-CoV-2 replication organelle and spatial link to vesicular-tubular compartment/Golgi apparatus located assembly sites. Related to Figure 4

Video S6. Vimentin remodeling in SARS-CoV-2 infected cell visualized by full-cell 3D STED microscopy. Related to Figure 5

Video S7. Live cell visualization of vimentin cage formation in SARS-CoV-2 infected cells. Related to Figure 5

References

Angelini, M.M., Akhlaghpour, M., Neuman, B.W., and Buchmeier, M.J. (2013). Severe acute respiratory syndrome coronavirus nonstructural proteins 3, 4, and 6 induce double-membrane vesicles. mBio *4*.

Beier, T., Pape, C., Rahaman, N., Prange, T., Berg, S., Bock, D.D., Cardona, A., Knott, G.W., Plaza, S.M., Scheffer, L.K.*, et al.* (2017). Multicut brings automated neurite segmentation closer to human performance. Nat Methods *14*, 101-102.

Belevich, I., Joensuu, M., Kumar, D., Vihinen, H., and Jokitalo, E. (2016). Microscopy Image Browser: A Platform for Segmentation and Analysis of Multidimensional Datasets. PLoS Biol *14*, e1002340.

Bouhaddou, M., Memon, D., Meyer, B., White, K.M., Rezelj, V.V., Correa Marrero, M., Polacco, B.J., Melnyk, J.E., Ulferts, S., Kaake, R.M.*, et al.* (2020). The Global Phosphorylation Landscape of SARS-CoV-2 Infection. Cell.

Chu, H., Chan, J.F.-W., Yuen, T.T.-T., Shuai, H., Yuan, S., Wang, Y., Hu, B., Yip, C.C.-Y., Tsang, J.O.-L., Huang, X.*, et al.* (2020). Comparative tropism, replication kinetics, and cell damage profiling of SARS-CoV-2 and SARS-CoV with implications for clinical manifestations, transmissibility, and laboratory studies of COVID-19: an observational study. The Lancet Microbe *1*, e14-e23.

Çiçek, Ö., Abdulkadir, A., Lienkamp, S.S., Brox, T., and Ronneberger, O. (2016). 3D U-Net: Learning Dense Volumetric Segmentation from Sparse Annotation. Paper presented at: Medical Image Computing and Computer-Assisted Intervention – MICCAI 2016 (Cham: Springer International Publishing).

Cook, K.C., Moreno, J.A., Jean Beltran, P.M., and Cristea, I.M. (2019). Peroxisome Plasticity at the Virus-Host Interface. Trends Microbiol *27*, 906-914.

Cortese, M., Goellner, S., Acosta, E.G., Neufeldt, C.J., Oleksiuk, O., Lampe, M., Haselmann, U., Funaya, C., Schieber, N., Ronchi, P.*, et al.* (2017). Ultrastructural Characterization of Zika Virus Replication Factories. Cell Rep *18*, 2113-2123.

Dixit, E., Boulant, S., Zhang, Y., Lee, A.S., Odendall, C., Shum, B., Hacohen, N., Chen, Z.J., Whelan, S.P., Fransen, M.*, et al.* (2010). Peroxisomes are signaling platforms for antiviral innate immunity. Cell *141*, 668-681.

Eriksson, J.E., He, T., Trejo-Skalli, A.V., Harmala-Brasken, A.S., Hellman, J., Chou, Y.H., and Goldman, R.D. (2004). Specific in vivo phosphorylation sites determine the assembly dynamics of vimentin intermediate filaments. J Cell Sci *117*, 919-932.

Gordon, D.E., Jang, G.M., Bouhaddou, M., Xu, J., Obernier, K., White, K.M., O'Meara, M.J., Rezelj, V.V., Guo, J.Z., Swaney, D.L.*, et al.* (2020). A SARS-CoV-2 protein interaction map reveals targets for drug repurposing. Nature *583*, 459-468.

Hagemeijer, M.C., Monastyrska, I., Griffith, J., van der Sluijs, P., Voortman, J., van Bergen en Henegouwen, P.M., Vonk, A.M., Rottier, P.J., Reggiori, F., and de Haan, C.A. (2014). Membrane rearrangements mediated by coronavirus nonstructural proteins 3 and 4. Virology *458-459*, 125-135.

879 Hanslovsky, P., Pisarev, I., Leite, V., Saalfeld, S., Funke, J., tpietzsch, Günther, U., Bogovic, J.,
880 Constantin, P., Schmidt, U., The Gitter Badger, Nunez-Iglesias, J. (2020). saalfeldlab/paintera paintera-
881 0.24.0 (Version paintera-0.24.0). Zenodo. http://doi.org/10.5281/zenodo.372486

883 Hennies, J., Lleti, J.M.S., Schieber, N.L., Templin, R.M., Steyer, A.M., and Schwab, Y. (2020). AMST:
884 Alignment to Median Smoothed Template for Focused Ion Beam Scanning Electron Microscopy Image
885 Stacks. Sci Rep *10*, 2004.

887 Hoffmann, M., Kleine-Weber, H., Schroeder, S., Kruger, N., Herrler, T., Erichsen, S., Schiergens, T.S.,
888 Herrler, G., Wu, N.H., Nitsche, A.*, et al.* (2020). SARS-CoV-2 Cell Entry Depends on ACE2 and
889 TMPRSS2 and Is Blocked by a Clinically Proven Protease Inhibitor. Cell *181*, 271-280 e278.

891 Huang, C., Wang, Y., Li, X., Ren, L., Zhao, J., Hu, Y., Zhang, L., Fan, G., Xu, J., Gu, X.*, et al.* (2020).
892 Clinical features of patients infected with 2019 novel coronavirus in Wuhan, China. Lancet *395*, 497-506.

894 Klein, S., Cortese, M., Winter, S.L., Wachsmuth-Melm, M., Neufeldt, C.J., Cerikan, B., Stanifer, M.L.,
895 Boulant, S., Bartenschlager, R., and Chlanda, P. (2020). SARS-CoV-2 structure and replication
896 characterized by in situ cryo-electron tomography. bioRxiv, 2020.2006.2023.167064.

898 Knoops, K., Kikkert, M., Worm, S.H., Zevenhoven-Dobbe, J.C., van der Meer, Y., Koster, A.J.,
899 Mommaas, A.M., and Snijder, E.J. (2008). SARS-coronavirus replication is supported by a
900 reticulovesicular network of modified endoplasmic reticulum. PLoS Biol *6*, e226.

902 Kremer, J.R., Mastronarde, D.N., and McIntosh, J.R. (1996). Computer visualization of three-dimensional
903 image data using IMOD. Journal of Structural Biology *116*, 71-76.

905 Lennemann, N.J., and Coyne, C.B. (2017). Dengue and Zika viruses subvert reticulophagy by NS2B3-
906 mediated cleavage of FAM134B. Autophagy *13*, 322-332.

908 Limaye, A. (2012). Drishti: a volume exploration and presentation tool, Vol 8506 (SPIE).

910 Lowe, D.G. (2004). Distinctive Image Features from Scale-Invariant Keypoints. International Journal of
911 Computer Vision *60*, 91-110.

913 Marzolini, C., Stader, F., Stoeckle, M., Franzeck, F., Egli, A., Bassetti, S., Hollinger, A., Osthoff, M.,
914 Weisser, M., Gebhard, C.E.*, et al.* (2020). Effect of Systemic Inflammatory Response to SARS-CoV-2 on
915 Lopinavir and Hydroxychloroquine Plasma Concentrations. Antimicrob Agents Chemother.

917 Mastronarde, D.N. (2005). Automated electron microscope tomography using robust prediction of
918 specimen movements. J Struct Biol *152*, 36-51.

920 Mastronarde, D.N., and Held, S.R. (2017). Automated tilt series alignment and tomographic
921 reconstruction in IMOD. J Struct Biol *197*, 102-113.

923 Mohan, R., and Bargagna-Mohan, P. (2016). Chapter Eight - The Use of Withaferin A to Study
924 Intermediate Filaments. In Methods in Enzymology, M.B. Omary, and R.K.H. Liem, eds. (Academic
925 Press), pp. 187-218.

927 Monel, B., Rajah, M.M., Hafirassou, M.L., Sid Ahmed, S., Burlaud-Gaillard, J., Zhu, P.P., Nevers, Q.,
928 Buchrieser, J., Porrot, F., Meunier, C.*, et al.* (2019). Atlastin Endoplasmic Reticulum-Shaping Proteins
929 Facilitate Zika Virus Replication. J Virol *93*.

930
931   Mostowy, S., and Shenoy, A.R. (2015). The cytoskeleton in cell-autonomous immunity: structural
932   determinants of host defence. Nat Rev Immunol *15*, 559-573.
933
934   Neufeldt, C.J., Cerikan, B., Cortese, M., Frankish, J., Lee, J.-Y., Plociennikowska, A., Heigwer, F.,
935   Joecks, S., Burkart, S.S., Zander, D.Y.*, et al.* (2020). SARS-CoV-2 infection induces a pro-inflammatory
936   cytokine response through cGAS-STING and NF-κB. bioRxiv, 2020.2007.2021.212639.
937
938   Neufeldt, C.J., Cortese, M., Scaturro, P., Cerikan, B., Wideman, J.G., Tabata, K., Moraes, T., Oleksiuk,
939   O., Pichlmair, A., and Bartenschlager, R. (2019). ER-shaping atlastin proteins act as central hubs to
940   promote flavivirus replication and virion assembly. Nat Microbiol *4*, 2416-2429.
941
942   Ogando, N.S., Dalebout, T.J., Zevenhoven-Dobbe, J.C., Limpens, R., van der Meer, Y., Caly, L., Druce,
943   J., de Vries, J.J.C., Kikkert, M., Barcena, M.*, et al.* (2020). SARS-coronavirus-2 replication in Vero E6
944   cells: replication kinetics, rapid adaptation and cytopathology. J Gen Virol.
945
946   Otsu, N. (1979). A Threshold Selection Method from Gray-Level Histograms. IEEE Transactions on
947   Systems, Man, and Cybernetics *9*, 62-66.
948
949   Oudshoorn, D., van der Hoeven, B., Limpens, R.W., Beugeling, C., Snijder, E.J., Barcena, M., and
950   Kikkert, M. (2016). Antiviral Innate Immune Response Interferes with the Formation of Replication-
951   Associated Membrane Structures Induced by a Positive-Strand RNA Virus. mBio *7*.
952
953   Pahmeier, F., Neufeldt, C.J., Cerikan, B., Prasad, V., Pape, C., Laketa, V., Ruggieri, A., Bartenschlager,
954   R., and Cortese, M. (2020). A versatile reporter system to monitor virus infected cells and its application
955   to dengue virus and SARS-CoV-2. bioRxiv, 2020.2008.2031.276683.
956
957   Pape, C., Remme, R., Wolny, A., Olberg, S., Wolf, S., Cerrone, L., Cortese, M., Klaus, S., Lucic, B.,
958   Ullrich, S.*, et al.* (2020). Microscopy-based assay for semi-quantitative detection of SARS-CoV-2 specific
959   antibodies in human sera. bioRxiv, 2020.2006.2015.152587.
960
961   Paul, D., and Bartenschlager, R. (2013). Architecture and biogenesis of plus-strand RNA virus replication
962   factories. World J Virol *2*, 32-48.
963
964   Perlman, S., and Masters, P.S. (2020). Coronaviridae: The viruses and their replication, Vol 1, 7th edn.
965
966   Sandoval, I.V., Bonifacino, J.S., Klausner, R.D., Henkart, M., and Wehland, J. (1984). Role of
967   microtubules in the organization and localization of the Golgi apparatus. J Cell Biol *99*, 113s-118s.
968
969   Schindelin, J., Arganda-Carreras, I., Frise, E., Kaynig, V., Longair, M., Pietzsch, T., Preibisch, S.,
970   Rueden, C., Saalfeld, S., Schmid, B.*, et al.* (2012). Fiji: an open-source platform for biological-image
971   analysis. Nat Methods *9*, 676-682.
972
973   Schneider, C.A., Rasband, W.S., and Eliceiri, K.W. (2012). NIH Image to ImageJ: 25 years of image
974   analysis. Nature Methods *9*, 671-675.
975
976   Schorb, M., Haberbosch, I., Hagen, W.J.H., Schwab, Y., and Mastronarde, D.N. (2019). Software tools for
977   automated transmission electron microscopy. Nat Methods *16*, 471-477.
978

979 Snijder, E.J., Limpens, R., de Wilde, A.H., de Jong, A.W.M., Zevenhoven-Dobbe, J.C., Maier, H.J., Faas,
980 F., Koster, A.J., and Barcena, M. (2020). A unifying structural and functional model of the coronavirus
981 replication organelle: Tracking down RNA synthesis. PLoS Biol *18*, e3000715.
982
983 Tang, D., Comish, P., and Kang, R. (2020). The hallmarks of COVID-19 disease. PLoS Pathog *16*,
984 e1008536.
985
986 Vergara, H.M., Pape, C., Meechan, K.I., Zinchenko, V., Genoud, C., Wanner, A.A., Titze, B., Templin,
987 R.M., Bertucci, P.Y., Simakov, O.*, et al.* (2020). Whole-body integration of gene expression and single-
988 cell morphology. bioRxiv, 2020.2002.2026.961037.
989
990 Wehland, J., Henkart, M., Klausner, R., and Sandoval, I.V. (1983). Role of microtubules in the
991 distribution of the Golgi apparatus: effect of taxol and microinjected anti-alpha-tubulin antibodies. Proc
992 Natl Acad Sci U S A *80*, 4286-4290.
993
994 Wolff, G., Limpens, R.W.A.L., Zevenhoven-Dobbe, J.C., Laugks, U., Zheng, S., de Jong, A.W.M.,
995 Koning, R.I., Agard, D.A., Grünewald, K., Koster, A.J.*, et al.* (2020). A molecular pore spans the double
996 membrane of the coronavirus replication organelle. bioRxiv, 2020.2006.2025.171686.
997
998 Wrapp, D., Wang, N., Corbett, K.S., Goldsmith, J.A., Hsieh, C.L., Abiona, O., Graham, B.S., and
999 McLellan, J.S. (2020). Cryo-EM structure of the 2019-nCoV spike in the prefusion conformation. Science
1000 *367*, 1260-1263.
1001 Yu, Y.T., Chien, S.C., Chen, I.Y., Lai, C.T., Tsay, Y.G., Chang, S.C., and Chang, M.F. (2016). Surface
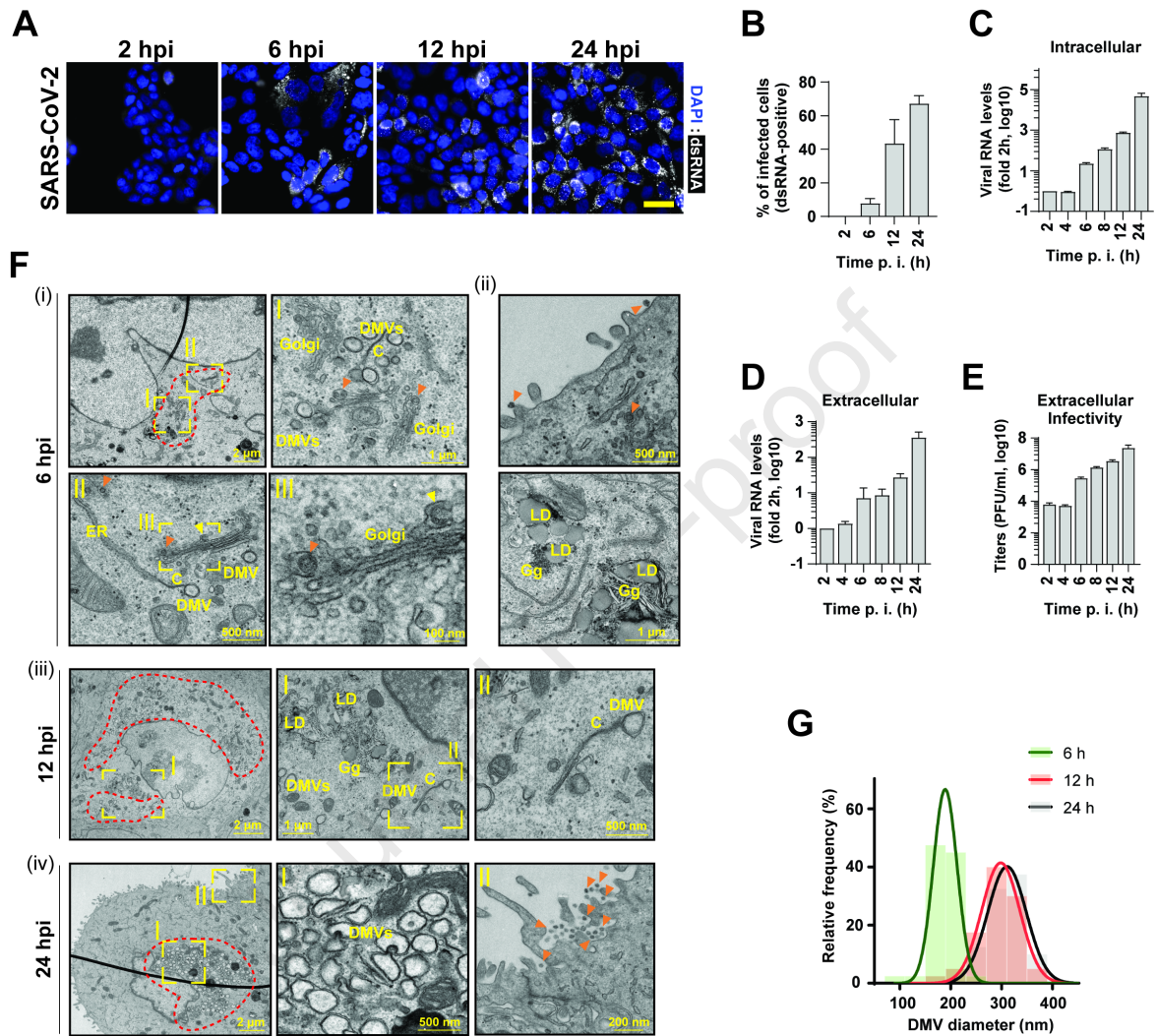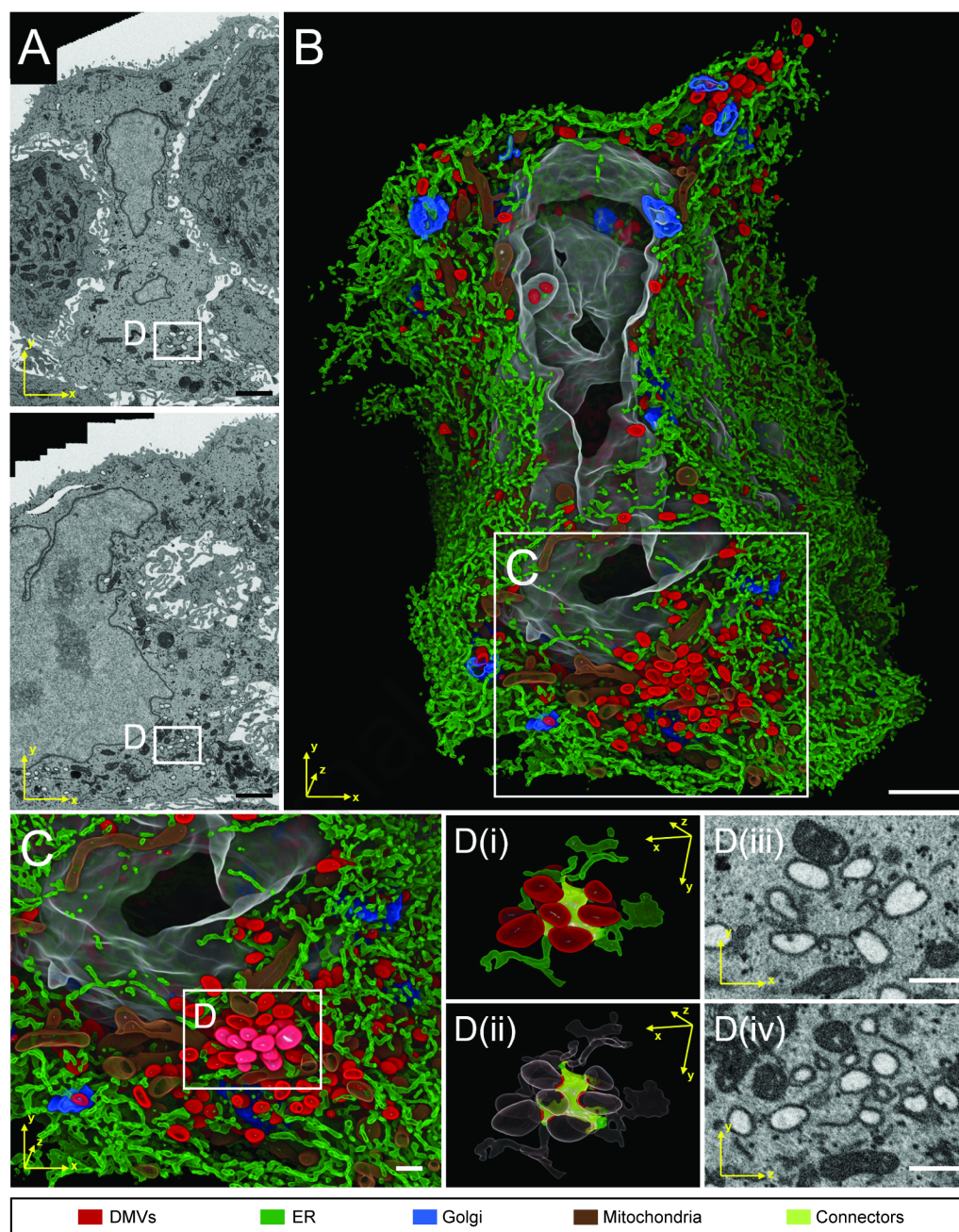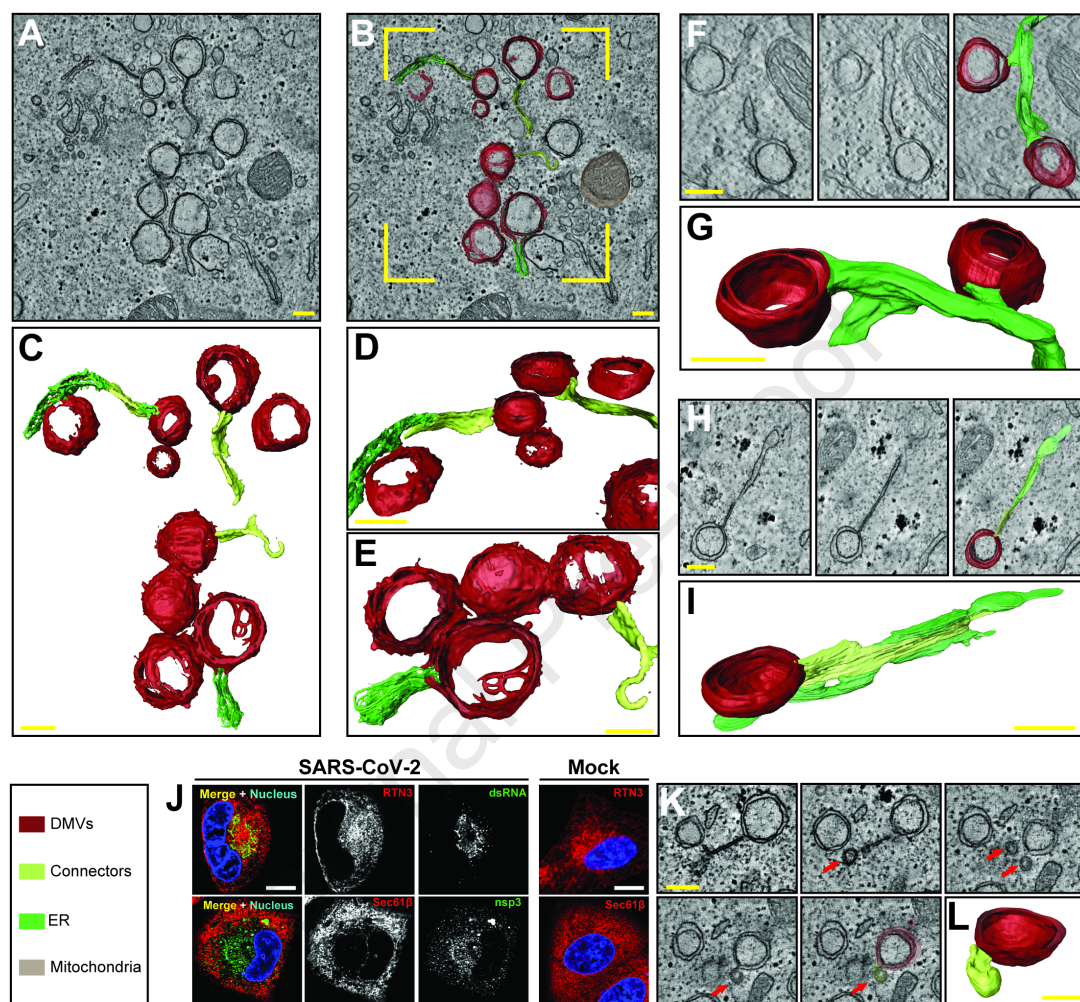1002 vimentin is critical for the cell entry of SARS-CoV. J Biomed Sci *23*, 14.
1003

Figure 1

| ■ DMVs | ■ ER | ■ Golgi | ■ Mitochondria | ■ Connectors |

Figure 2

Figure 3

Assembled Virions	DMVs	ER	Golgi	Mitochondria
Budding Virions	Connectors	VTC	Lysosomes	Peroxisomes

G

SARS-CoV-2

Golgi (GM130)
Nuclei dsRNA

Golgi (GM130)

2 hpi   6 hpi   12 hpi   24 hpi

Mock
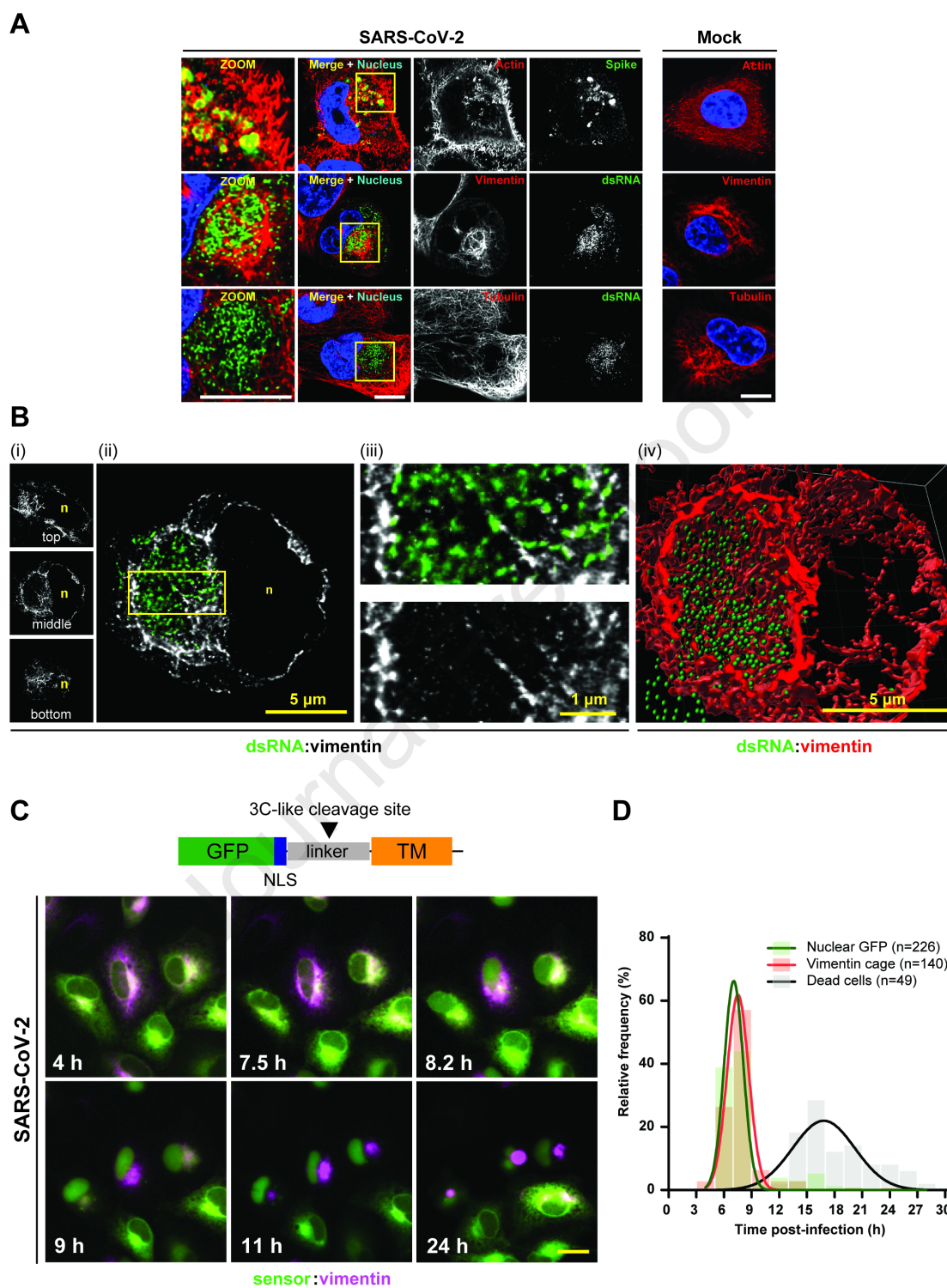
H

Figure 4

A

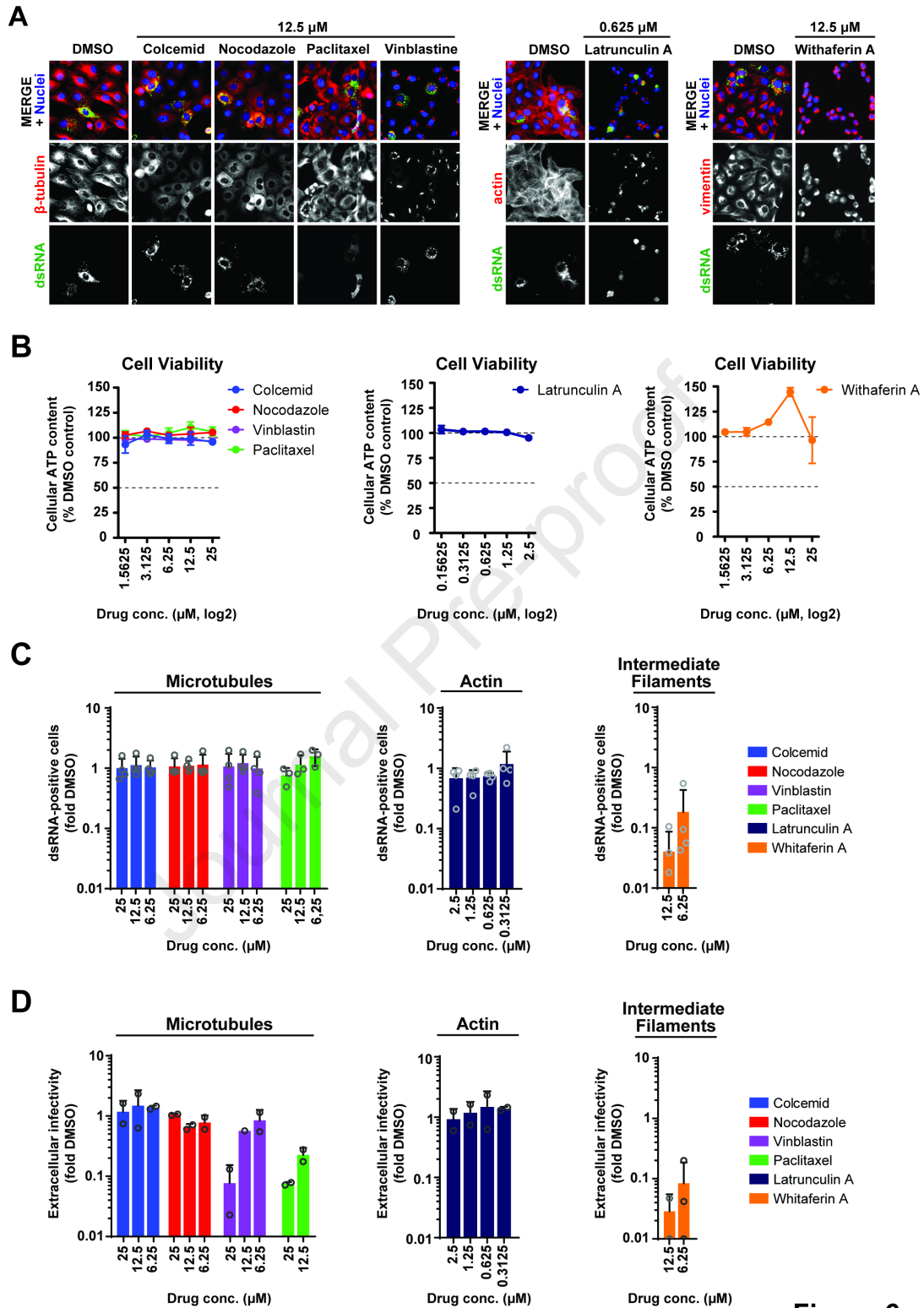

B

C

D
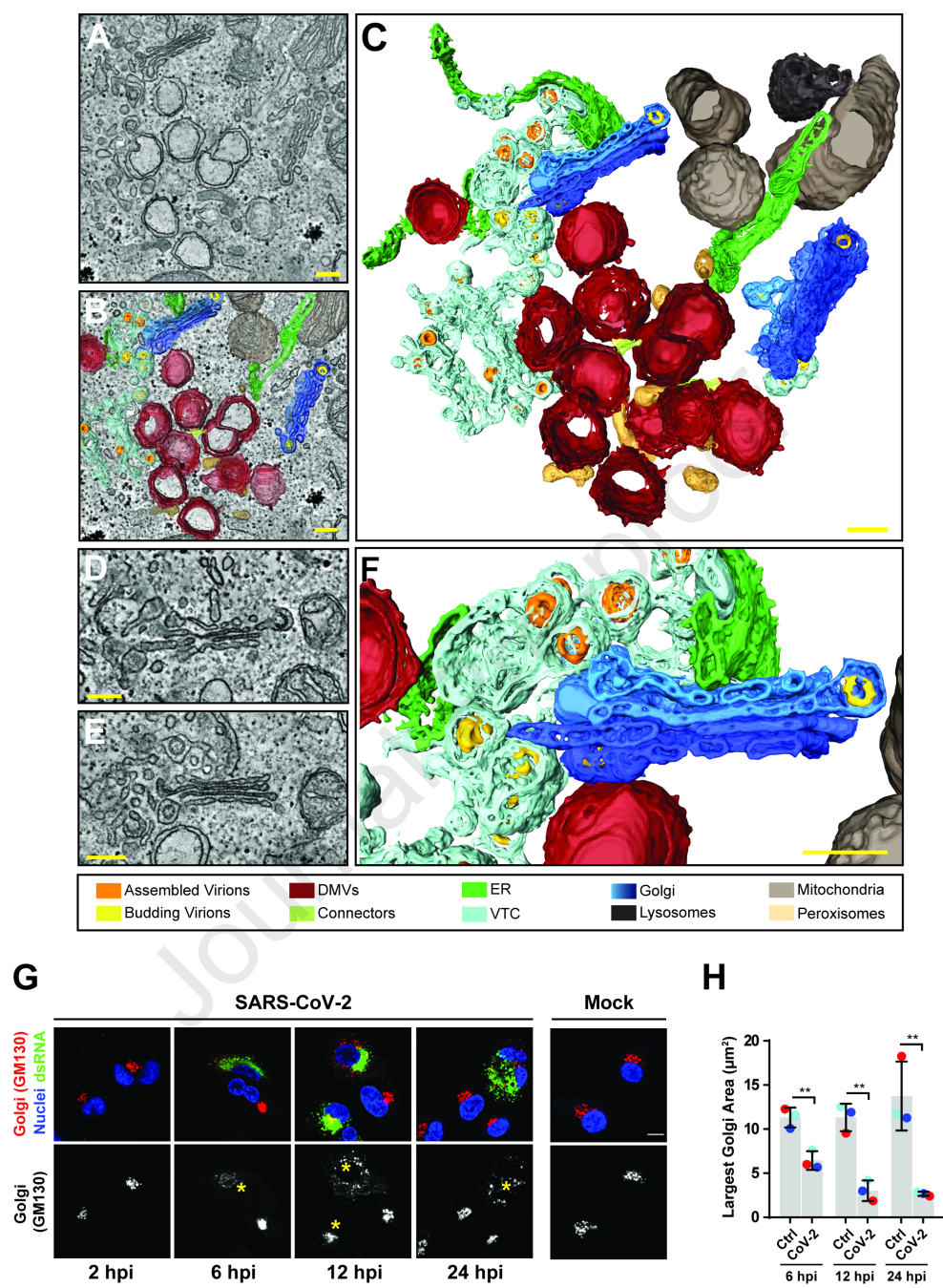
Figure 5

Figure 6

Highlights

- Integrative imaging approaches reveal SARS-CoV-2 induced cellular alterations
- SARS-CoV-2 extensively remodels the cellular endomembrane system
- Pharmacological inhibition of cytoskeleton remodeling restricts viral replication
- We provide a comprehensive repository of virus-induced ultrastructural cell changes

eTOC Blurb

Cortese et al. use integrative imaging techniques to generate a publicly available repository of morphological alterations induced by SARS-CoV-2 in lung cells. Accumulation of ER-derived double membrane vesicles, the viral replication organelle, occurs concomitantly with cytoskeleton remodeling and Golgi fragmentation. Pharmacological alteration of cytoskeleton dynamics restricts viral replication and spread.